

Parametric analysis of masonry arches following a limit analysis approach: Influence of joint friction, pier texture, and arch shallowness

Mathematics and Mechanics of Solids
1–29

© The Author(s) 2023

Article reuse guidelines:

sagepub.com/journals-permissions

DOI: 10.1177/10812865231175385

journals.sagepub.com/home/mms



Alejandro Jimenez Rios 

Structural Engineering Research Group (SERG), Department of Built Environment (DBE), Faculty of Technology, Art and Design (TKD), Oslo Metropolitan University (OsloMet), Oslo, Norway

Bledian Nela 

Department of Structural and Geotechnical Engineering, Sapienza University of Rome, Rome, Italy

Marco Pingaro 

Department of Structural and Geotechnical Engineering, Sapienza University of Rome, Rome, Italy

Emanuele Reccia 

Department of Environmental Civil Engineering and Architecture, University of Cagliari, Cagliari, Italy

Patrizia Trovalusci 

Department of Structural and Geotechnical Engineering, Sapienza University of Rome, Rome, Italy

Received 13 January 2023; accepted 23 April 2023

Abstract

Among the most characteristic structures in historical constructions for crossing large spans are the masonry vaulted structures by utilizing their geometric stability to safely transfer the loads to supports with regard to their negligible tensile strength. The ability of masonry piers to bear such transferred stresses and safely convey them to the support is directly related to their structural integrity, as well as to a number of other factors. Using an in-house limit analysis code, a study on the crucial parameters impacting the safety level of piers under the thrust of arches is performed. Parameters such as pier texture, joint friction angle, and arch shallowness, namely, shallow, semi-circular, and pointed arches, were investigated under three load scenarios: horizontal and concentrated vertical live load applied at mid-span and quarter-span. The main findings of this work show that all studied parameters have a significant influence on the structure response. Higher friction values, sharper arches, and piers that follow the rule of art result in higher collapse

Corresponding author:

Patrizia Trovalusci, Department of Structural and Geotechnical Engineering, Sapienza University of Rome, Via Gramsci 53, 00197 Rome, Italy.
Email: patrizia.trovalusci@uniroma1.it

multipliers. Furthermore, this work emphasizes the importance of accounting for the sliding mechanism and masonry texture, parameters that are often neglected.

Keywords

Limit analysis, friction, no-tension contacts, arch shallowness, pier texture

1. Introduction

Arches over piers are typically encountered in various masonry architectural styles. Particularly, this combination of elements is quite common among Romanesque churches [1, 2]; Gothic cathedrals [3], churches [4], and monasteries [5]; Byzantine architecture [6]; medieval castles [7]; colonial [8, 9] and baroque churches [10, 11]; and uncountable smaller structures built along human history [12].

An interesting study case of this masonry typology is the one corresponding to the UNESCO World Heritage List of Matera in Italy [13] (see Figure 1(a)), a site where the seismic events had been previously underestimated by the normative until more accurate soil exploration studies have been recently performed [14]. The particular structural features of Matera buildings are the very thin vaults covering relatively large spaces supported by multi-leaf masonry piers. Few “*through stones*” (in Italian “*diatoni*”) and several voids are commonly found within the masonry piers internal structure of Matera constructions. Those piers usually sustain up to two levels of 5- to 6-m span vaults with of approximately 25 cm, also built with similar poor masonry assemblages [15] (see Figure 1(b)). In such cases, the piers are required to perform in a monolithic manner to sustain the thrust and safely transmit it to the foundations.

Another outstanding example of such structures can be found among the settlements of Anavatos (ca. 11th century) in the Greek island of Chios [16], which is a national listed monument. One- and two-story masonry buildings in Anavatos were covered by single or successive masonry domes (see Figure 1(c)). These buildings commonly had a rectangular layout of 4.5 by 7 m and were built next to each other with the aim of improving the lateral resistance of individual units. Many of these structures have been devastated by rheological factors, lack of maintenance, and natural disasters such as earthquakes and anthropological interventions (i.e. vandalism). In Figure 1(d), the internal arrangement of a typical masonry wall unit with a lack of structural integrity is shown. Moreover, Efesiou [16] provided insight of the original inclusion of perimetric and cross timber ties as structural reinforcement. Unfortunately, most of those elements were removed and used as firewood by the last inhabitants of the citadel, thus increasing the earthquake vulnerability of the remaining buildings.

Baggio and Trovalusci [15] highlighted the importance that the so-called “*rule of art*” had in the sound structural behaviour of such structures. They clearly show the influence that the structural integrity of the pier has on the global behavior of the structure when subjected to in-plane actions, vertical or horizontal. Giuffré and Carocci [18] demonstrate that one of the major causes for the necessary interventions in the case of Matera was the horizontal displacement of the walls due to the thrust. As well, Carocci [19] points out the crucial importance of the internal arrangement of the masonry wall in its thickness when subjected to the horizontal forces triggering the out-of-plane collapse. Additionally, three different approaches were suggested while designing conservation interventions on the historical centers in order to recover the original “*rule of art*” state of such constructions. According to Carocci, damaged masonry due to unduly interventions should be repaired by removing the alterations of the original material and restoring their interlocking to adjacent walls, cracked walls should be simply sealed by the means of compatible injections and plastering, and finally, heavily damaged masonry walls should be rebuilt by adopting the “*like for like*” (from Italian “*scuci-cuci*”) methodology following original construction technique guidelines.

The collapse mechanisms that could appear in an arch over piers, also called a buttressed arch, could be classified into three groups [20]:

- Local: where hinges appear only within the arch.
- Semi-global: where besides from the hinges at the arch, one hinge develops at the base of one of the piers.
- Global: where hinges appear within the arch and both piers.

Local mechanisms mainly appear in the presence of bulky piers ($H/B < 1$, where H represents pier height, and B corresponds to pier base), global mechanisms are typical of slender buttresses, and semi-global mechanisms commonly arise for intermediate piers geometries. Alexakis and Makris [12] discussed the possibility of

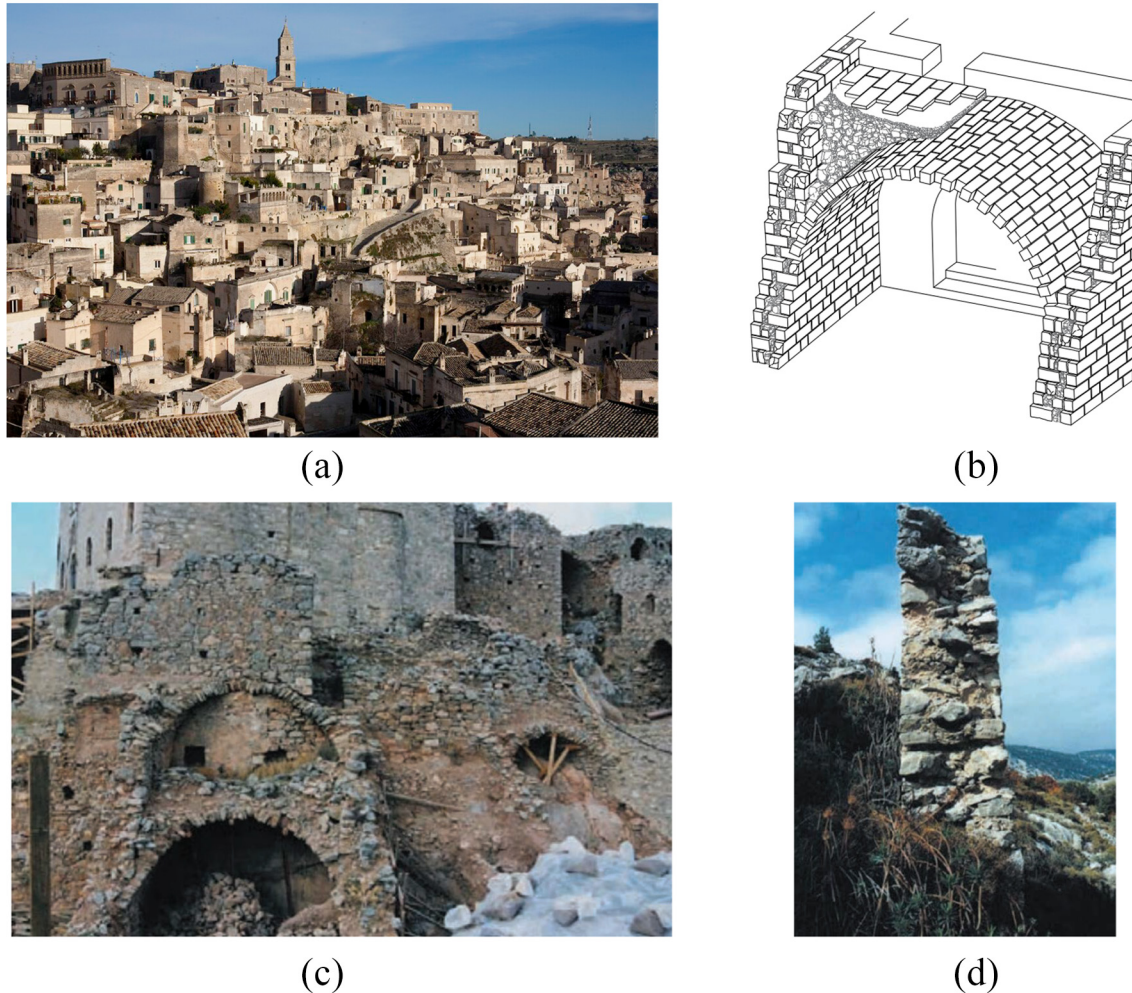


Figure 1. (a) The Sassi and the Park of Rupestrian Churches of Matera (Italy), Author: Valerio Li Vigni, taken from the UNESCO World Heritage Convention website [17]. (b) Example of a Matera masonry vault, representative of the arch over piers typology (reproduced from the work by Giuff 'e and Carocci [18]). (c) Successive domes in Anavatos (Chios island, Greece; ca. 11th century) [16]. (d) Internal masonry structure of walls in Anavatos [16].

encountering five physically admissible hinging mechanisms (among which a mechanism involving two hinges in a single pier was proposed), but this number could be even higher if sliding between masonry blocks is accounted for as done on the analysis performed by Jiménez et al. [21].

Pulatsu et al. [22] assessed the seismic performance of monolithic and regularly coursed dry-joint masonry piers supporting several arch forms under lateral loads proportional to the structures' mass. Moreover, they also examined the influence of steel tie-rod reinforcement on the studied masonry models. Those complex arch systems were simulated through a discrete element modeling (DEM) approach using the commercial software, 3DEC, in which masonry units were modeled as distinct blocks with zero tensile strength at their joints. Results revealed that pointed arches provided better seismic resistance than the circular arch form. Moreover, the implementation of steel tie-rods resulted on significant increase in stability for the arch-pier structures.

The curvature of an arch has a direct influence on the thrust that the element exerts at the arch-pier connection. It is well known that the higher the curvature of the arch is, the less horizontal thrust it exerts on the piers. This observation clearly affects the buttress design. Monolithic piers and pointed arches resulted in higher collapse multipliers in comparison with discrete piers and circular arches. In terms of collapse mechanism, a four-hinge failure mode developed. Three hinges were located along the arches, whereas the fourth one appeared at the base of the pier (located on the side of the arch corresponding to the horizontal load direction).

The application of the steel-tie reinforcement resulted in higher collapse multipliers for all the different arch geometries and pier typologies. It is noted that this increment was higher for circular arches than for pointed ones. Furthermore, in terms of collapse mechanism, the inclusion of the tie also affected the outcome. For the case of reinforced arch-pier structures, again a four-hinge mechanism developed, this time involving both piers.

Dimitri et al. [23] carried out a systematic DEM parametric analysis to assess the dynamic response and strength of multi-drum columns and arches on buttresses subjected to step and harmonic base impulses. For the latter case, arches were circular and buttresses were either monolithic or discrete. Other studied parameters were the inter-block friction value, the geometrical proportions, the impulse shape, and the inclusion of spandrel infill.

Counter-intuitively, the models with discrete buttresses resulted in higher dynamic resistances in comparison with the monolithic ones for short duration impulses (< 0.4 s). This phenomenon is explained based on the collapse mechanism typologies observed. While the monolithic buttresses models yielded a rocking collapse mechanism, the discrete buttresses presented a combined rocking–sliding mechanism, which allowed higher levels of energy dissipation during the mentioned impulse range. For long duration impulses, the dynamic resistance of both types of models was practically identical, and it tended to match the static solution of the problem.

The friction value variation had no effect whatsoever for the monolithic buttresses models, whereas that a slight resistance increment was detected for the higher friction values adopted on the discrete buttresses models (although this resistance improvement was only noticed during the short impulse duration range, < 0.4 s). On the other hand, the presence of spandrel infill caused a resistance decrease for all the models studied. This is explained by the fact that the destabilizing horizontal loads are higher than the expected stabilizing vertical weights. Furthermore, inter-block sliding of the spandrel units may result in higher thrust levels transferred at the buttresses, thus leading to weaker structures under the dynamic loads studied.

Bagi [24] demonstrates that the Safe Theorem of Heyman may not always hold, and that even if sliding is not considered, a system of rigid blocks may collapse although an equilibrated system of forces is found. Providing some examples Bagi demonstrates cases when it fails and as such proposes the need for an improved formulation of the theorem emphasizing the importance of the consideration of frictional forces in the system as non-Heymanian approach.

Hua and Milani [25, 26] propose a limit analysis approach to enable a simple modeling of masonry reinforced arches. They present the differences and drawbacks in considering the associated flow rule. Formulating both the associated and non-associated problem, where the former is implemented through linear programming (LP) and the latter through the sequential linear programming (SLP) scheme proposed by Gilbert et al. [27], they study the behavior of a segmental masonry arch within the lower bound and upper bound theorems. Considering the SLP scheme in each iteration, Gilbert et al. adjust the limit surface and thus gradually removing the dilatancy angle. Additionally, they emphasize the overestimation achieved when considering the associated flow rules that have an impact when assessing large-size problems. Hua and Milani perform further studies for the cases of reinforced masonry arches by simplifying it with no sliding restriction [25] and considering it [26]. Full and local reinforcements were analyzed where the importance of non-associated sliding was stressed out.

Zampieri et al. [28] implemented a thrust line analysis using the virtual work principle in order to study the structural response masonry piers supporting circular arches subjected to support settlements. Their approach followed the well-known Heyman assumption of no sliding between elements (infinite contact shear strength). For the case of masonry arches supported by buttresses subjected to a support settlement, only three hinges are required to form a collapse mechanism.

They found that the principal parameters affecting the stability of those kinds of structures were the settlement angle and arch slenderness. Furthermore, they highlighted the higher susceptibility of the pier-arch assemblies to horizontal displacements in comparison with vertical or inclined support movements.

Nela et al. [29, 30] implemented an upper-bound limit analysis numerical approach to study the structural response of partially reinforced masonry arches over masonry piers. They achieve to model the influence of the reinforcement by means of increased inter-block interfaces' cohesion values. Furthermore, they also studied the effect that arch sharpness had on the collapse multipliers and mechanisms of the structures while not considering geometrical or mechanical properties for the piers (a gap that is intended to be covered by this paper.)

In terms of both collapse mechanisms and multipliers, Nela et al. found a perfect agreement for the unreinforced scenarios in comparison with the DEM results reported by Pulatsu et al. [22]. Moreover, they stated that the tie-bar reinforcement proposed by Pulatsu et al. was more effective for semi-circular arches and slightly

pointed arches. On the other hand, the partial reinforcement strategy with composites resulted in higher collapse multiplier values than the one with a tie-bar for sharper pointed arches.

Dimitri and Tornabene [31] investigated the structural behaviour of circular, pointed, and basket-handle (three-centered) buttressed arches by the means of limit analysis analytical and DEM approaches. They found a good correlation with both analyses, thus validating the use of DEM to assess the condition of masonry arches over piers. Dimitri et al. concluded that buttressed pointed arches presented higher resistance than circular ones in the case of either local or semi-global collapse mechanisms formation. On the other hand, basket-handle buttressed arches with small embrace angles (120° and 150°) exhibited a weaker behavior than circular buttressed arches, whereas that for large embrace angles (180°), three-centered buttressed arches were more stable than their circular counterparts.

Alternative numerical approaches and methodologies have been developed by other authors. For example, triumphal arches, a slight variation of buttressed arches or arches over piers, were studied by De Luca et al. [20] with a simplified FEM-LA combined approach and their results were validated against non-linear detailed FEM models. Milani [32] formulated a new lower-bound finite element limit analysis for double-curved masonry and validated it with some examples. It proved to be very practical for the materials with almost null tensile strength and the outcomes provide efficiency and robustness of this approach when applied to masonry structures with double curvature but not limited. Building upon the well-established Heyman's [33–35] assumptions regarding unreinforced masonry behavior, DeJong and Ochsendorf [36] studied the structural response of masonry arches on buttresses using two different approaches, namely, thrust-line analysis and DEM. Similarly, Brandonisio et al. [37] and Brandonisio and De Luca [38] applied Heyman's hypothesis to develop an analytical model and study the behavior of buttressed arches, a model that was validated by comparing its results against values obtained by the means of DEM. Another important issue when dealing with curved masonry supported on piers is the settlements and Tiberti et al. [39] using a genetic algorithm–adaptive homogeneous approach represented the crack patterns induced by ground settlements on masonry walls.

Other aspects regarding the structural response of buttressed arches have been deduced by other authors as well. Just to name a few, Coccia et al. [40] studied the effect of support displacement through an analytical tool capable of computing the support displacement magnitude that would lead to collapse and of assessing the arch thrust value at that stage. They also considered the influence of pier height and concluded that accounting for support displacement is of paramount importance, especially for slender piers, as it greatly affects the stability of the structure.

Not many researchers deal with the texture of piers and among the few to do so were Alexakis and Makris [12]. They studied piers with only horizontal joints (horizontal rupture) and discretized piers where a diagonal crack could develop (elongation failure). One of the limitations of this study though is the fact that they implemented Heyman's assumptions, thus only rotation hinges could develop within their analyzed models. The numerical approach developed by Alexakis and Makris was based on the principle of stationary potential energy and it was validated in comparison with the results obtained through a DEM approach.

The main contribution of this work intends to include the crucial aspect of the inter-block sliding in the behavior of buttressed arches, in contrast to the many studies under Heyman assumptions that neglect this effect. Utilizing the specialized upper-bound limit analysis approach through the in-house code entitled ALMA 2.1, a study of the pier texture effect in the global response of masonry arches with different rise considering diverse level of friction at the joints is performed.

The rest of this paper is organized such as in section 2 the theoretical formulation behind the numerical approach used to carry out the simulations presented in this paper is detailed, while in section 3, the parametric analysis performed is presented where three main parameters were analyzed, namely, arch sharpness, inter-block contact friction, and pier texture. In section 4, the results obtained from the parametric analysis in terms of collapse multipliers and collapse mechanisms are presented followed by a corresponding discussion. Finally, in section 5, the main conclusions drawn from this work are highlighted.

2. Methodology: the ALMA code

The upper-bound LA approach implemented in the ALMA 2.1 software and used in this work is based on the notation and theoretical formulation originally proposed by Baggio and Trovalusci [41, 42]. Within this framework, masonry arches (and other masonry structures) are described as a system of n blocks and m joints. Masonry blocks are rigid with no-tension and frictional joints and the sliding resistance is described through the coefficient of friction, $\tan(\phi)$, where ϕ is the friction angle. In 2D simulations, the blocks can undergo two kinds

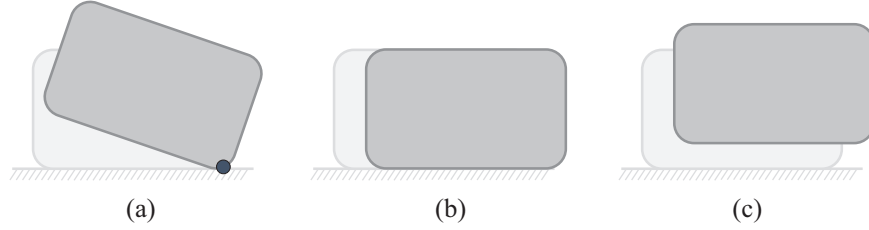


Figure 2. Schematic representation of possible mechanisms for one-block structure: (a) rotation, (b) sliding, and (c) sliding (dilatant behavior).

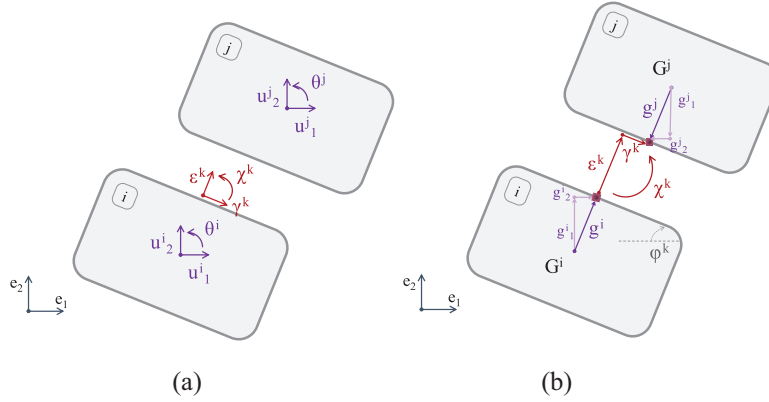


Figure 3. Schematic representation of a two-block structure with one joint represented in the local reference system: (a) kinematic variables and (b) geometric quantities.

of motion: translation (sliding) and rotation about their edges (hinging) as shown in Figure 2(a)–(c), respectively. Moreover, in ALMA 2.1, sliding assumes a dilatant behavior (Figure 2(c)). Hereon vectors are denoted by bold lowercase letters, matrices by bold uppercase letters, and scalar entities by non-bold letters.

2.1. Kinematic compatibility

Considering a 2D space with the orthonormal basis $\mathbf{e} = \{e_1, e_2\}^T$, generalized infinitesimal displacements at block centroids are denoted by the vector $\mathbf{u}^i = \{u_1^i, u_2^i, \theta^i\}^T$, which contains the displacement components u_1 , u_2 , and the rotation θ (Figure 3(a)). The \mathbf{u} ($\in \mathcal{R}^{3n}$) vector collects all single vectors of individual blocks' generalized displacements.

The kinematic variables such as the relative normal displacement (ε^k), relative tangential displacement (γ^k), and relative rotation (χ^k) kinematic components of every k th joint are organized into a vector $\boldsymbol{\varepsilon}^k = \{\varepsilon^k, \gamma^k, \chi^k\}^T$. The vector $\boldsymbol{\varepsilon}$ ($\in \mathcal{R}^{3m}$) collects all the single vectors into the global vector of generalized strains, as shown in Figure 3(b).

Kinematic compatibility of the system is constructed by applying a rotational matrix that maps the local joint coordinates of arbitrarily directed coordinates to the global system. In the reference configuration, middle edge points of contact surfaces coincide. Therefore, for a k th joint between two blocks i th and j th, kinematic inter-compatibility assumes the following form:

$$\begin{cases} \varepsilon^k = -\sin(\varphi^k)u_1^i + \cos(\varphi^k)u_2^i + \left(g_1^{i,k} \cos(\varphi^k) + g_2^{i,k} \sin(\varphi^k)\right)\theta^i + \\ \quad + \sin(\varphi^k)u_1^j - \cos(\varphi^k)u_2^j - \left(g_1^{j,k} \cos(\varphi^k) + g_2^{j,k} \sin(\varphi^k)\right)\theta^j, \\ \gamma^k = \cos(\varphi^k)u_1^i + \sin(\varphi^k)u_2^i + \left(g_1^{i,k} \sin(\varphi^k) - g_2^{i,k} \cos(\varphi^k)\right)\theta^i + \\ \quad - \cos(\varphi^k)u_1^j - \sin(\varphi^k)u_2^j - \left(g_1^{j,k} \sin(\varphi^k) - g_2^{j,k} \cos(\varphi^k)\right)\theta^j, \\ \chi^k = \theta^i - \theta^j, \end{cases} \quad (1)$$

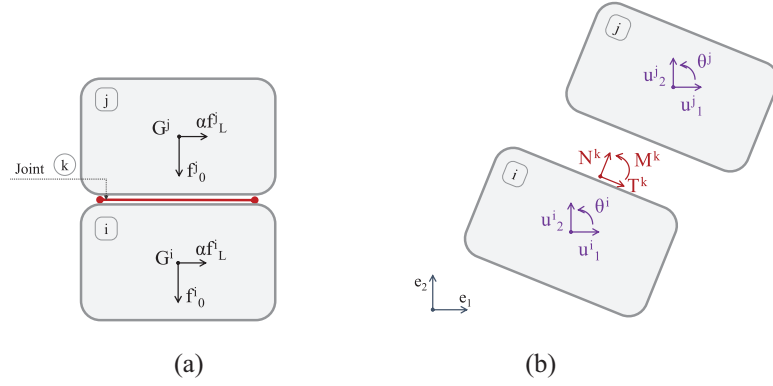


Figure 4. Schematic representation of a two-block structure with one joint represented in the local reference system: (a) dead and live loads and (b) static variables.

where φ^k is the inclination angle of the joints as shown in Figure 3(b). Thus, equations (1) for the whole system read as:

$$\epsilon = \mathbf{B} \mathbf{u} . \quad (2)$$

where \mathbf{B} represents the compatibility matrix of the system. The \mathbf{B} matrix for the 2D case is a linear transform $\mathcal{R}^{3n} \rightarrow \mathcal{R}^{3m}$. If the null space of the compatibility matrix for the homogeneous system has a zero dimension, then equation (2) can be written in the following form:

$$\begin{aligned} \epsilon_1 &= \mathbf{B}_1 \mathbf{u} , \\ \epsilon_2 &= \mathbf{B}_2 \mathbf{u} , \end{aligned} \quad (3)$$

where \mathbf{B}_1 is the kinematic submatrix with a maximum rank of $(3n)$ as a linear transform $\mathcal{R}^{3n} \rightarrow \mathcal{R}^{3n}$ and \mathbf{B}_2 is the rest of the kinematic matrix as a linear transform $\mathcal{R}^{3n} \rightarrow \mathcal{R}^{3(m-n)}$. Vectors ϵ_1 ($\in \mathcal{R}^{3n}$) and ϵ_2 ($\in \mathcal{R}^{3(m-n)}$) represent the vector of the free generalized strains and vector of the linearly dependent strains, respectively. Utilizing the Gauss–Jordan transform and after some algebraic operations the solution takes the form:

$$\begin{aligned} \mathbf{u} &= \mathbf{A}_0 \epsilon_1 , \\ \epsilon_2 &= \mathbf{A} \epsilon_1 , \end{aligned} \quad (4)$$

where \mathbf{A} and \mathbf{A}_0 substitute $\mathbf{B}_2 \mathbf{B}_1^{-1}$ and \mathbf{B}_1^{-1} , respectively.

2.2. Equilibrium

In the considered 2D space, the system of n blocks is subjected to a couple of loads applied in their respective centroid of mass, where for each i th rigid block:

$$\mathbf{f}^i = \mathbf{f}_0^i + \alpha \mathbf{f}_L^i , \quad \text{with } i = 1, \dots, n , \quad (5)$$

where $\mathbf{f}_0^i = \{f_{01}^i, f_{02}^i, m_0^i\}^T$ and $\mathbf{f}_L^i = \{f_{L1}^i, f_{L2}^i, m_L^i\}^T$ represent the dead and live load vectors, respectively. Live loads are proportional to the dead loads through a non-negative load multiplier, α (see Figure ??). Analogous to the global generalized displacement vector, the global load vector \mathbf{f} ($\in \mathcal{R}^{3n}$) is obtained collecting the single load vectors \mathbf{f}^i .

Moreover, at every k th joint, a triad of normal force (N^k), shear force (T^k), and moment (M^k) components is present, thus forming the static variables of the joint (see Figure 4(b)). These forces are assembled into a global vector of generalized stress σ ($\in \mathcal{R}^{3m}$). Likewise, the generalized stresses are represented in a local system at every k th joint σ^k , as shown in Figure 4(b). The equation of equilibrium for the entire system now reads as follows:

$$\mathbf{B}^T \sigma + \mathbf{f} = \mathbf{0} . \quad (6)$$

For the vector of generalized loads \mathbf{f} from equation (6), using the principle of the virtual work and applying equilibrium the following equation is obtained:

$$\mathbf{f} \mathbf{u} + \boldsymbol{\sigma} \boldsymbol{\epsilon} = \mathbf{0}. \quad (7)$$

After introducing the vectors of generalized contact actions, $\boldsymbol{\sigma}_1$ that works on the free generalized strains $\boldsymbol{\epsilon}_1$ and $\boldsymbol{\sigma}_2$ that works on the linearly dependent generalized strains $\boldsymbol{\epsilon}_2$, equation (7) takes the following form:

$$\mathbf{f} \mathbf{u} + \boldsymbol{\sigma}_1 \boldsymbol{\epsilon}_1 + \boldsymbol{\sigma}_2 \boldsymbol{\epsilon}_2 = \mathbf{0}. \quad (8)$$

Substitution of the solution for generalized displacements from equation (4) and considering equation (5) of the generalized load, further algebraic operations yield the following equation:

$$\boldsymbol{\sigma}_1 + \mathbf{A}^T \boldsymbol{\sigma}_2 + \mathbf{A}_0^T (\mathbf{f}_0 + \alpha \mathbf{f}_L) = \mathbf{0}. \quad (9)$$

2.3. Yield domain

The generalized yield domain of the system is formulated as

$$\mathbf{y} = \mathbf{N}^T \boldsymbol{\sigma} \leq \mathbf{0}, \quad (10)$$

where N represents the gradient matrix of the adopted failure surface. The gradient matrix N for the 2D case is a linear transform $\mathcal{R}^{3m} \rightarrow \mathcal{R}^{4m}$. For every k th joint, equation (10) assumes the following form:

$$\begin{cases} y_1^k = l^k/2N^k - M^k; \\ y_2^k = l^k/2N^k + M^k, \\ y_3^k = \tan(\phi)N^k - T^k; \\ y_4^k = \tan(\phi)N^k + T^k, \end{cases} \quad (11)$$

where l^k is the length of k th joint. In the same analogy for the free $\boldsymbol{\sigma}_1$ ($\mathcal{R}^{3n} \rightarrow \mathcal{R}^{4m}$) and linearly dependent $\boldsymbol{\sigma}_2$ ($\mathcal{R}^{3(m-n)} \rightarrow \mathcal{R}^{4m}$) generalized contact actions, the following inequality is obtained for the yield domain:

$$\mathbf{y} = \mathbf{N}_1^T \boldsymbol{\sigma}_1 + \mathbf{N}_2^T \boldsymbol{\sigma}_2 \leq \mathbf{0}. \quad (12)$$

2.4. Flow rule

The flow rule expresses the generalized vector of strains, $\boldsymbol{\epsilon}$, as a linear combination of non-negative coefficients, $\boldsymbol{\lambda}$ (also known as plastic multipliers) of four modes for the 2D case. This relationship can be written as

$$\boldsymbol{\epsilon} = \mathbf{M} \boldsymbol{\lambda}, \quad (13)$$

where \mathbf{M} is the matrix containing the modes of failure as a linear transform $\mathcal{R}^{4m} \rightarrow \mathcal{R}^{3m}$. For every k th joint, equation (13) assumes the following form:

$$\begin{cases} \varepsilon_1^k = l^k/2 \lambda_1 + l^k/2 \lambda_2, \\ \gamma_2^k = -\lambda_3 + \lambda_4, \\ \chi_3^k = -\lambda_1 + \lambda_2. \end{cases} \quad (14)$$

In the same analogy for the free $\boldsymbol{\epsilon}_1$ ($\mathcal{R}^{4m} \rightarrow \mathcal{R}^{3n}$) and linearly dependent $\boldsymbol{\epsilon}_2$ ($\mathcal{R}^{4m} \rightarrow \mathcal{R}^{3(m-n)}$) generalized strains, the following inequality is obtained for the yield domain:

$$\begin{aligned} \boldsymbol{\epsilon}_1 &= \mathbf{M}_1 \boldsymbol{\lambda}, \\ \boldsymbol{\epsilon}_2 &= \mathbf{M}_2 \boldsymbol{\lambda}, \end{aligned} \quad (15)$$

2.5. Complementarity and positive work of the live loads

Within the domain of holonomic perfect plasticity where there is neutral proportional loading with no unloading, remaining on the yield surface is only permitted for positive values of the plastic multipliers. Therefore, reaching an admissible collapse mechanism, this requirement is satisfied imposing Prager's consistency (complementarity) condition provided in equation (16). In this condition, it is ensured that positive plastic multipliers $\lambda \neq 0$ generate plastic collapse only for $\mathbf{y} = 0$, whereas in the case of $\mathbf{y} \neq 0$, plastic collapse does not occur as $\lambda = 0$.

$$\boldsymbol{\lambda}^T \cdot \mathbf{y} = 0. \quad (16)$$

As a final condition, the collapse mechanism is characterized by the non-negative work of the live loads that is normalized [43] and expressed in equation (17).

$$\mathbf{f}_L^T \cdot \mathbf{u} = 1. \quad (17)$$

2.6. The non-associative optimization problem formulation

In the presence of non-associative friction, the relations shown characterize the problem of non-standard rigid-plastic materials. The main outcomes to be resolved from the above-formulated problem is the factor α which as stated is the load multiplier as a proportional load coefficient. So far the equations that govern the problem of the entire structure for the non-associative case can be summarized as follows:

$$\begin{aligned} \text{Kinematic compatibility: } & \boldsymbol{\epsilon} = \mathbf{B} \mathbf{u}, \\ \text{Equilibrium: } & \mathbf{B}^T \boldsymbol{\sigma} = \mathbf{f}_0 + \alpha \mathbf{f}_L, \\ \text{Yield domain: } & \mathbf{y} = \mathbf{N}^T \boldsymbol{\sigma} \leq \mathbf{0}, \\ \text{Flow rule: } & \boldsymbol{\epsilon} = \mathbf{M} \boldsymbol{\lambda}, \\ \text{Positive live load: } & \mathbf{f}_L^T \cdot \mathbf{u} = 1, \\ \text{Consistency condition: } & \boldsymbol{\lambda}^T \cdot \mathbf{y} = 0. \end{aligned} \quad (18)$$

In the case of non-standard materials, that is, materials with non-associated flow rule, the postulate of Drucker [44] is not valid and normality rule does not hold, which yields a non-unique solution. Among the first ones to notice the solution non-uniqueness was Coulomb [45]. Nevertheless, as per the "*Friction Theorems*" of Drucker [46], the solution set of statically and kinematically admissible load multipliers is bounded. In this case, the solution set of collapse load multipliers α_c of a system containing non-associative frictional joints is contained within a upper boundary of a collapse multipliers considering joints with dilatancy and a lower boundary of collapse multipliers considering frictionless joints. After performing algebraic operations on equations (4), (9), (12) and (15)–(17), the NLP problem can be expressed as follows:

$$\begin{aligned} \alpha_c = \min.\{\alpha\} \quad \text{subjected to:} \\ (\mathbf{A}\mathbf{M}_1 - \mathbf{M}_2) \boldsymbol{\lambda} = \mathbf{0}, \\ -\boldsymbol{\lambda}^T \cdot (\mathbf{N}_1 \mathbf{A}_0)^T (\mathbf{f}_0 + \alpha \mathbf{f}_L) + \boldsymbol{\lambda}^T \cdot (\mathbf{N}_2 - \mathbf{N}_1 \mathbf{A})^T \boldsymbol{\sigma}_2 \leq \mathbf{0}, \\ -(\mathbf{N}_1 \mathbf{A}_0)^T (\mathbf{f}_0 + \alpha \mathbf{f}_L) + (\mathbf{N}_2 - \mathbf{N}_1 \mathbf{A})^T \boldsymbol{\sigma}_2 \leq \mathbf{0}, \\ \boldsymbol{\lambda}^T (\mathbf{A}_0 \mathbf{M}_1)^T \cdot \mathbf{f}_L - 1 = 0, \\ \alpha \geq 0, \quad \boldsymbol{\lambda} \geq \mathbf{0}, \end{aligned} \quad (19)$$

where consecutively equations (19) represent conditions of kinematic compatibility, static admissibility, non-linear complementarity, and normalized positive live loads, with the bounds on the unknowns α and $\boldsymbol{\lambda}$ on the last expression.

The programming problem obtained consists of an NLP-constrained minimization problem and the main issues with the solution is that it is often trapped in a local minimum far from the global one leading to incorrect collapse multiplier. To avoid this obstacle, Baggio and Trovalusci [41] suggested a two-step procedure where the LP solution (described in the next section) from the first step is used as the initial estimate for the solution of the NLP on the second step.

2.7. The associative optimization problem formulation

Drucker [46] showed that for assemblages with non-associated flow rules, the bounds on the multiplier, namely lower and upper, can be determined. Considering the Radenkovic [47] theorem, the lower bound for the multiplier as described by the equations in the previous sections is equivalent to the ultimate multiplier of the system with actual flow rule provided in equation (15) that is associated with a yield surface $\hat{y} = \mathbf{0}$, but the surface in this case is the plastic potential and it serves such as to define $\mathbf{M}^T = \partial \hat{y} / \partial \boldsymbol{\sigma}$. Whereas the upper bound of the multiplier is equivalent to the ultimate multiplier for the system with the actual flow rule and associated with the yield surface of equation (12) and the associated flow rule that is defined from $\mathbf{M} = \partial y / \partial \boldsymbol{\sigma} = \mathbf{N}$. The latter corresponds to the collapse load of a system with frictional and dilatant interfaces. The problem can be linearized when considering the actual yield surfaces, but by correcting the direction of vector $\boldsymbol{\lambda}$ to be associated with that surface, and this was achieved by Baggio and Trovalusci [42] replacing the friction angle with dilatancy.

In this case, the problem is linearized and can be solved using a linear mathematical programming. From the previous section this serves as the initial estimate for the two-step procedure; however, the effectiveness in terms of accuracy of the solution with respect to the number of unknowns (as provided in the work by Baggio and Trovalusci [41]), comparing NLP and LP results, is not so distinct, and in the case of parametric analysis, only the relative influencing parameters are significant.

Therefore, considering a dilatant behaviour for the joints, yield surface remains the same as the non-associative case but by modifying the modes of failure matrix \mathbf{M} , after replacement of friction angle with dilatancy, it is equalized with the gradient matrix \mathbf{N}

$$\mathbf{M} = \mathbf{N} , \quad (20)$$

signifying the plastic flow is associated with the yield surface and the normality rule holds. Now the relations in equation (14) take the following form

$$\begin{cases} \varepsilon_1^k = l^k/2 \lambda_1 + l^k/2 \lambda_2 + \tan(\phi)\lambda_3 + \tan(\phi)\lambda_4, \\ \gamma_2^k = -\lambda_3 + \lambda_4, \\ \chi_3^k = -\lambda_1 + \lambda_2, \end{cases} \quad (21)$$

and consecutively equation (15) is expressed as follows:

$$\begin{aligned} \boldsymbol{\epsilon}_1 &= \mathbf{N}_1 \boldsymbol{\lambda} , \\ \boldsymbol{\epsilon}_2 &= \mathbf{N}_2 \boldsymbol{\lambda} . \end{aligned} \quad (22)$$

The adopted kinematic upper bound problem is defined (in terms of a LP) as

$$\begin{aligned} \alpha_c = \min \{ & -\boldsymbol{\lambda}^T (\mathbf{A}_0 \mathbf{N}_1)^T \mathbf{f}_0 \} \quad \text{subjected to:} \\ & (\mathbf{A} \mathbf{N}_1 - \mathbf{N}_2) \boldsymbol{\lambda} = \mathbf{0}, \\ & \boldsymbol{\lambda}^T (\mathbf{A}_0 \mathbf{N}_1)^T \mathbf{f}_L - 1 = 0, \\ & \boldsymbol{\lambda} \geq \mathbf{0}, \end{aligned} \quad (23)$$

in which equation (23) is consecutively the condition of compatibility and normalized positive work of the live loads with the last expression giving the bounds on the unknowns for $\boldsymbol{\lambda}$.

Recently, ALMA 2.1 has been enriched with the possibility of assigning different values of cohesion to every joint to account for particular tensile and shear strength values at every block interface. This feature, in addition to the various already available software capabilities of ALMA 2.1, namely, foundation settlement [48] and retrofitting tie modeling [49], has been validated with other literature examples in the work by Nela [29, 30]. Cohesion is accounted by modifying the yield domain as shown in Figure 5, where in blue are given the yield domains including cohesion for both rotation (a) and sliding (b). Equation (24) describes this generalized domain:

$$\mathbf{y} = \mathbf{N}^T \boldsymbol{\sigma} + \mathbf{c} \leq \mathbf{0} , \quad (24)$$

Thus, the objective function of the LP, equation (23), is transformed into

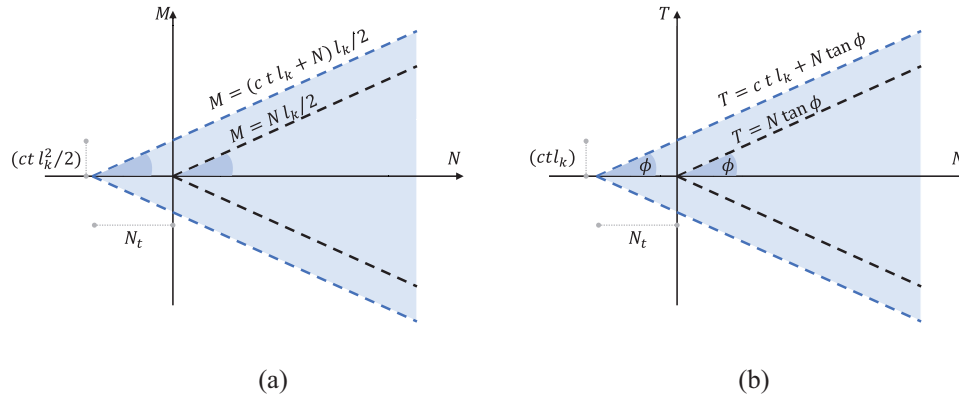


Figure 5. Implemented Mohr-Coulomb yield domain with and without cohesion for (a) bending and (b) shear.

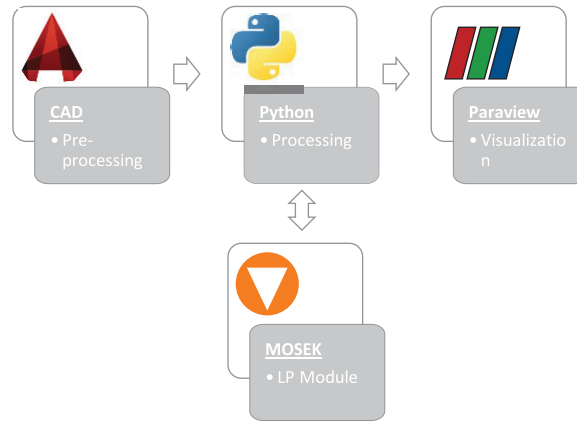


Figure 6. General structure of the ALMA code modules.

$$\alpha_c = \min \{ \lambda^T [c - (A_0 N_1)^T] f_0 \}, \quad (25)$$

where the different cohesion values assigned to every joint of the masonry assemblage are stored in the form of a vector c . A Mohr–Coulomb classical yield domain is considered with the inclusion of cohesion, thus indirectly involving tensile strength of the joints.

2.8. Code structure

A general structure of the code including the main modules is given in Figure 6. In this manner the code utilizes as processor *Python*TM programming language where for the LP optimization problem the *MOSEK*[®] [50] library is used for the solution. The in-built optimization libraries in *Python*TM such as *SciPy* can be used as well, but *MOSEK*[®] provides a more stable and faster solution. Pre-processing is carried out in a *CAD* environment where the blocks are created using closed polygons indicating the intersection joints and on this wise the joints of contact. Finally, post-processing is executed inside *Python*TM which outputs the collapse multiplier, whereas the collapse mechanism is visualized with the help of the open source code *Paraview* [51].

3. Parametric analysis description

In this paper, the influence that three main factors have in the structural behavior of buttressed arches is studied. A full composite design has been implemented; in other words, all levels of every factor have been combined with each other, which has resulted in a relatively large pool of numerical simulations. Taking advantage of the relatively fast computations by applying the limit analysis approach, the simulations are performed within a reasonable amount of time (average time per analysis was 21 s with a maximum of 44 s).

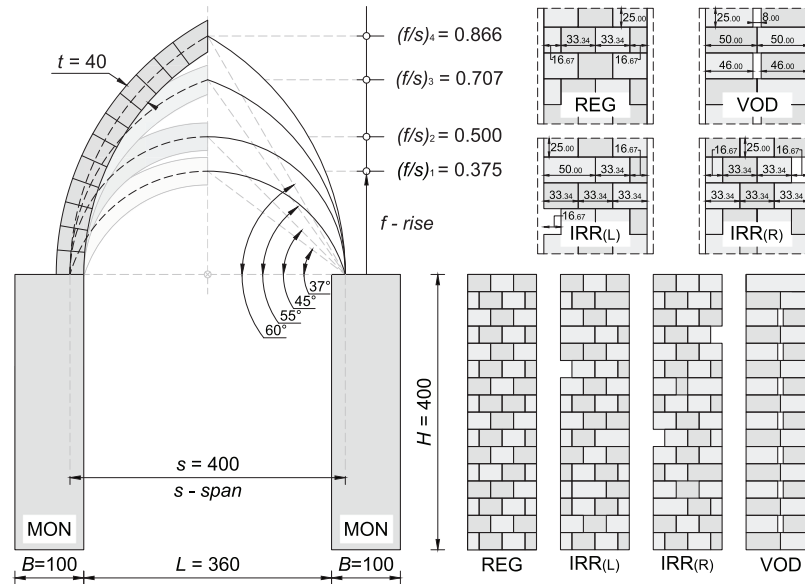


Figure 7. Different levels of the arch shallowness and pier texture parameters (dimensions in cm).

The first factor is purely geometry related and it has to do with the shape of the arch. A shallow arch, a semi-circular arch, and two pointed arches have been taken into account. This factor is herein referred to as the *arch shallowness*. The values assigned to arch shallowness correspond to the ratio between the arch rise (f) and the arch span (s) (see Figure 7). As many authors have previously pointed out [52–55], pointed arches exert lower values of horizontal thrust at their springs in comparison with semi-circular and shallow arches. When they are supported by piers, this phenomenon plays a paramount role as to how that horizontal thrust is absorbed by the buttresses and transferred to the foundations of the structure.

The second parameter, friction, is a mechanical one and has to do with the surface shape of the masonry blocks. The surface contact between blocks of a dry masonry structure, or of one with highly decayed mortar as typically found on historical buildings, highly influences the response of the assembly. Friction is described by the so-called friction angle, ϕ , whose values in practice usually range between 15° and 63° [56] (although theoretically, those values could be between 0° and 90°). Therefore, common friction coefficient values, $\tan \phi$, range between 0.27 and 1.96. Common friction angle values on historical masonry structures can be found between 15° and 45° ; thus, for this study it has been decided to adopt 20, 30, and 40 as the levels for the friction factor.

The pier texture factor could be seen as a combination between geometry and mechanical properties. Throughout the history of masonry construction, it has been well known that the *rule of art*, which was developed after a long series of trial and errors and that traditionally passed from master to apprentice, played a paramount role on the structural stability and soundness of masonry structures. Thus, the geometrical arrangement of the masonry blocks influences the mechanical properties of the structural elements built with this material and provides a better interlocking within them yielding various levels of tensile strength for the masonry [57]. The ideal case in this paper is idealized as a monolithic pier where in theory the *rule of art* is followed “*verbatim*” and the quality and strength of the mortar is such that crack opening among the blocks of the pier is prevented. A second pier texture case is idealized as a regularly arrangement of the masonry blocks at the pier. Then, two cases of idealized damaged or ill-built piers are considered, namely, one with irregular texture and another one with internal voids (see Figure 7). On the other hand, pier dimensions are kept constant throughout this study, as the focus is placed on pier texture only, and not on pier geometry itself.

Furthermore, three different load scenarios have been analyzed. In the first one, a proportional horizontal live load is applied to the entire masonry assembly, whereas that for the other two cases, a concentrated proportional vertical live load has been applied at mid and quarter span, respectively (relative to the weight of two arch blocks for the mid span and three for the quarter span). All load scenarios also take into account the vertical self-weight of the buttressed arches. ALMA code possesses the possibility to consider the vertical loading of the infill or

other actions (infill considerations with ALMA have been previously studied [29]); in this study, they have been neglected to observe the pure structural behavior of the arch.

Therefore, four different pier textures, four different arch geometries, three different levels of friction value, and three different load scenarios have been combined in the study presented in this paper. This has given rise to the creation and simulation of a total 144 models studied utilizing the limit analysis approach. Note that for the sake of simplicity of the figure captions, an acronym system has been created for each type of analysis. The acronym follows a sequence of "texture_shallowness_friction." Texture takes attributes such as *MON*—monolithic, *REG*—regular, *IRR*—irregular, and *VOD*—with voids. Shallowness takes attributes as 375—shallow, 500—semi-circular, 707—pointed, and 866—very pointed arches. Friction takes attributes following the angle of friction such as 20—low level, 30—medium level, and 40—high level. For example, the acronym "*MON_707_30*" refers to the pointed arch supported on monolithic piers considering a friction angle of 30°.

4. Results and discussion

As mentioned in the previous section, a total of 144 models were created and analyzed. In order to simplify the analysis of the results, all the collapse multipliers and collapse mechanisms obtained have been grouped by load scenario. Collapse multipliers are presented as box plots in combination with swarm plots. For every load scenario, three box/swarm plots are included (one for each parameter analyzed, namely, pier texture, arch shallowness, and friction value). In each one of these plots, "*minimum*" and "*maximum*", as well as first quartile (Q1), median, and third quartile (Q3), are displayed along with all the individual values of the collapse multipliers obtained. Outlier values are shown as black rhomboids in those figures as well.

Beside the use of IQR, a full factorial design of experiment has been performed to assess not only the statistical significance of each of the parameters but also their internal interaction. The outcomes of this analysis have been summarized in a Pareto chart of the standardized effects with a confidence level of 95%. From this chart it is easy to evaluate which of the parameters have a significant effect on the response, in this case the collapse multiplier, based on the threshold given marked with the red dashed line. Additional information about the design of experiment can be found in the work by Rios et al. [55] where they perform this statistical study. Whereas the available raw data of the numerical simulations performed for all the cases are available in [59–61].

4.1. Collapse multipliers for the horizontal live load case

From Figure 8(a) clear positive relationship can be observed between friction and arch shallowness with respect to the collapse multiplier values obtained. In other words, the higher the value of friction angle and arch shallowness, the higher would be the collapse multiplier. Moreover, we can see that the quality of the pier texture also plays an important role on the strength of masonry buttressed arches. Higher collapse multiplier values were found for the cases of monolithic and regular texture piers, both of which comply with the so-called "*rule of art*." On the other hand, the idealized irregular and voids pier texture models, which are idealizations of ill-built or damaged/decayed structures, provided lower collapse multiplier values. These observations are in agreement with similar results reported in the literature and reinforce the concept of the importance that masonry texture and the adequate implementation of the "*rule of art*" has on the stability of such structural typologies.

Other inferences could be made based on the information summarized in Figure 8. The spread of the data obtained could be also analyzed to estimate the variability that could be expected if the methodology presented in this paper would be used to analyze other masonry structures based on the parameters studied in this research. Several data spread measurement tools are available, namely, range, standard deviation, and interquartile range ($IQR = Q3 - Q1$). It has been decided to use the IQR for such purposes due to the fact that the presence of outliers may affect the estimation of the other two quantities.

Thus, it could be noted that weaker pier textures (irregular and voids) present higher variability (data spread) with respect to sound pier textures (monolithic and regular) as the box sizes (IQR) of the former are larger than those of the latter. This collapse multiplier values variation is almost identical for the different levels of the arch shallowness parameter (slightly higher for the shallow arches group in comparison with the pointed arches one with a shallowness value of 0.866). On the other hand, the variability obtained for the different friction levels is clearly observed. Higher variability was found for the low-friction value group in contrast to the lower variability of the high-friction value group (intermediate variability for the medium-friction value group).

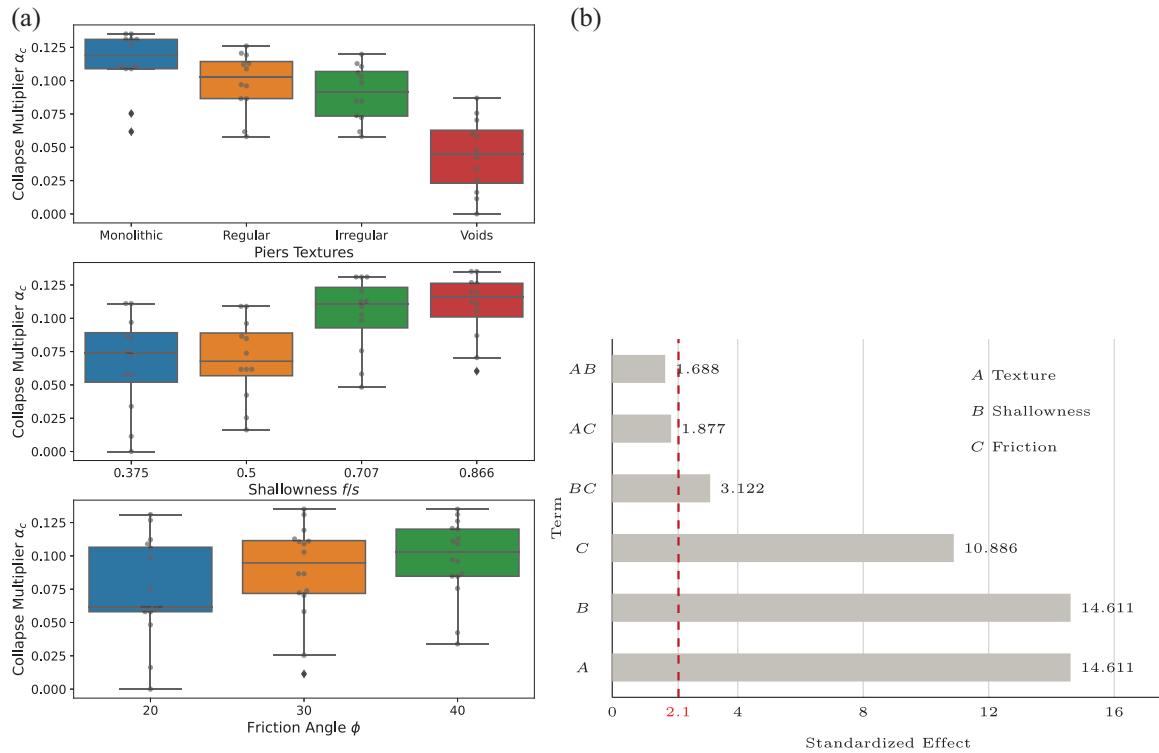


Figure 8. (a) Box plot and swarm plot of all collapse multipliers and (b) the Pareto chart of standardized effects for the horizontal live load case.

Table 1. Interquartile ranges (IQRs) for all parameter levels for the horizontal live load case

Parameter	Level	IQR	Mean	Coef. var.	Min.	Max.
Piers textures	Monolithic	0.02201	0.11393	0.20858	0.06173	0.13509
	Regular	0.02779	0.09882	0.22535	0.05808	0.12608
	Irregular	0.03350	0.09049	0.23017	0.05808	0.11989
	Voids	0.03977	0.04409	0.62109	0.00001	0.08692
Shallowness f/s	0.866	0.02528	0.10904	0.22403	0.06030	0.13509
	0.707	0.03041	0.10263	0.27335	0.04827	0.13100
	0.500	0.03208	0.06903	0.43837	0.01624	0.10899
	0.375	0.03713	0.06663	0.54309	0.00001	0.11104
Friction angle ϕ	40	0.03530	0.09793	0.29990	0.03392	0.13509
	30	0.03964	0.08852	0.39990	0.01142	0.13509
	20	0.04840	0.07404	0.50461	0.00001	0.13100

IQR values for all the levels of the parameters studied under the horizontal live load scenario are presented in Table 1.

The two outliers observed for the monolithic piers (see Figure 8) correspond to the shallow and semi-circular arch models with low-friction values. The outlier corresponding to the pointed arches group, 0.866, is related to the voids pier texture with low-friction model. Finally, the outlier of the medium-friction value group has to do with the voids texture piers and shallow arch model. Thus, low- to medium-friction values in combination with poor-quality piers (voids) and shallow arches may result, in some real-life structure cases, in lower collapse multiplier values than it may be expected. Masonry structures with this combination of critical values should be given special consideration by practitioners studying and designing interventions to preserve them.

Similarly, looking at the Pareto chart in Figure 8(b) with the threshold at 2.1, it can be easily observed that each single term of this chart has a significant importance with texture being the highest. Regarding two-way interactions, the highest significance obtained is the one related to the combination friction-shallowness.

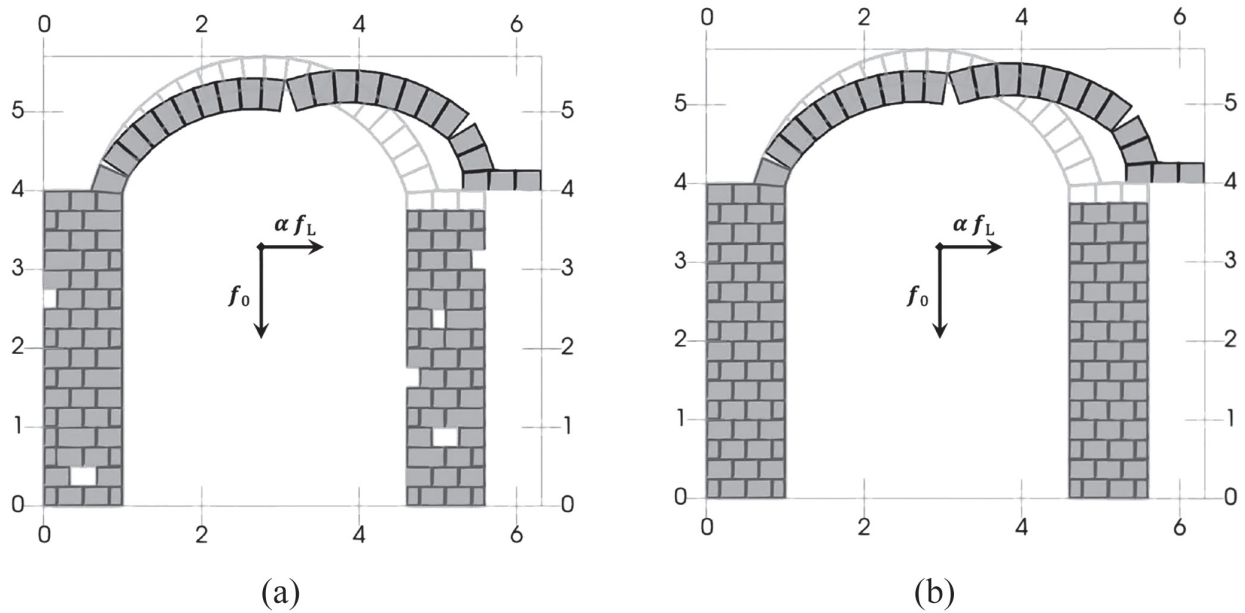


Figure 9. Combined collapse mechanisms involving hinging at the arch and sliding at the first pier row of blocks (grid in m): (a) IRR_375_20 and $\alpha_c = 0.0581$ and (b) REG_375_20 and $\alpha_c = 0.0581$.

4.2. Collapse mechanisms for the horizontal live load case

In terms of failure modes, four different collapse mechanisms were observed for the horizontal live load case models:

- Combined hinging at the arch and sliding at the first blocks course of the pier.
- Combined hinging at the arch and sliding at the arch springs.
- Combined hinging at both arch and pier plus sliding at the arch near its key.
- Pure hinging at both arch and pier.

It is important to highlight at this point that the special upper-bound limit analysis implementation applied on this paper has allowed to capture the first three types of failure mode involving sliding of the blocks (and also the failure modes involving sliding of the other two load cases presented hereafter on this paper). This would have not been possible if pure Heyman's assumptions would have been adopted as was done in the past by previous works [12, 28, 36–38]. This is in fact one of the main contributions of this paper to the advance of knowledge and understanding regarding masonry failure phenomena.

The first failure mode observed for the buttressed arches subjected to a horizontal live load is characterized by a rotation hinge at the intrados near the spring of the arch, a second rotation hinge at the extrados near the arch key, followed by a third rotation hinge at the intrados near the opposite spring of the arch and sliding of the entire top course of blocks at the top of the pier (see Figure 9). This collapse mechanism cannot develop on the monolithic pier models (as monolithic piers are not discretized). Furthermore, it is typical of shallow arches, which exert a relatively high horizontal thrust at the arch springs, in combination with low-friction values, which are not high enough to prevent the sliding of the blocks receiving the thrust from the arch and transfer those forces to lower block courses and incorporate the pier texture. Regardless of the pier discretization assumption, either irregular or regular texture, the collapse multiplier value obtained is the same for this failure mode ($\alpha = 0.0581$), which is the lowest of all α values computed for the buttressed arches subjected to horizontal live load analyzed in this study.

The second type of collapse mechanism observed involved only the arch (see Figure 10). It is formed by two intrados rotation hinges near each of the arch springs, an extrados rotation hinge close the arch key, and sliding of the arch at one of its springs. The piers do not interact in this failure mode. Thus, regardless of the pier discretization, whether it is irregular, regular, or monolithic, the same collapse multiplier is found ($\alpha = 0.0617$ for the semi-circular arch cases and $\alpha = 0.0754$ for the shallow arch model). Similar to the

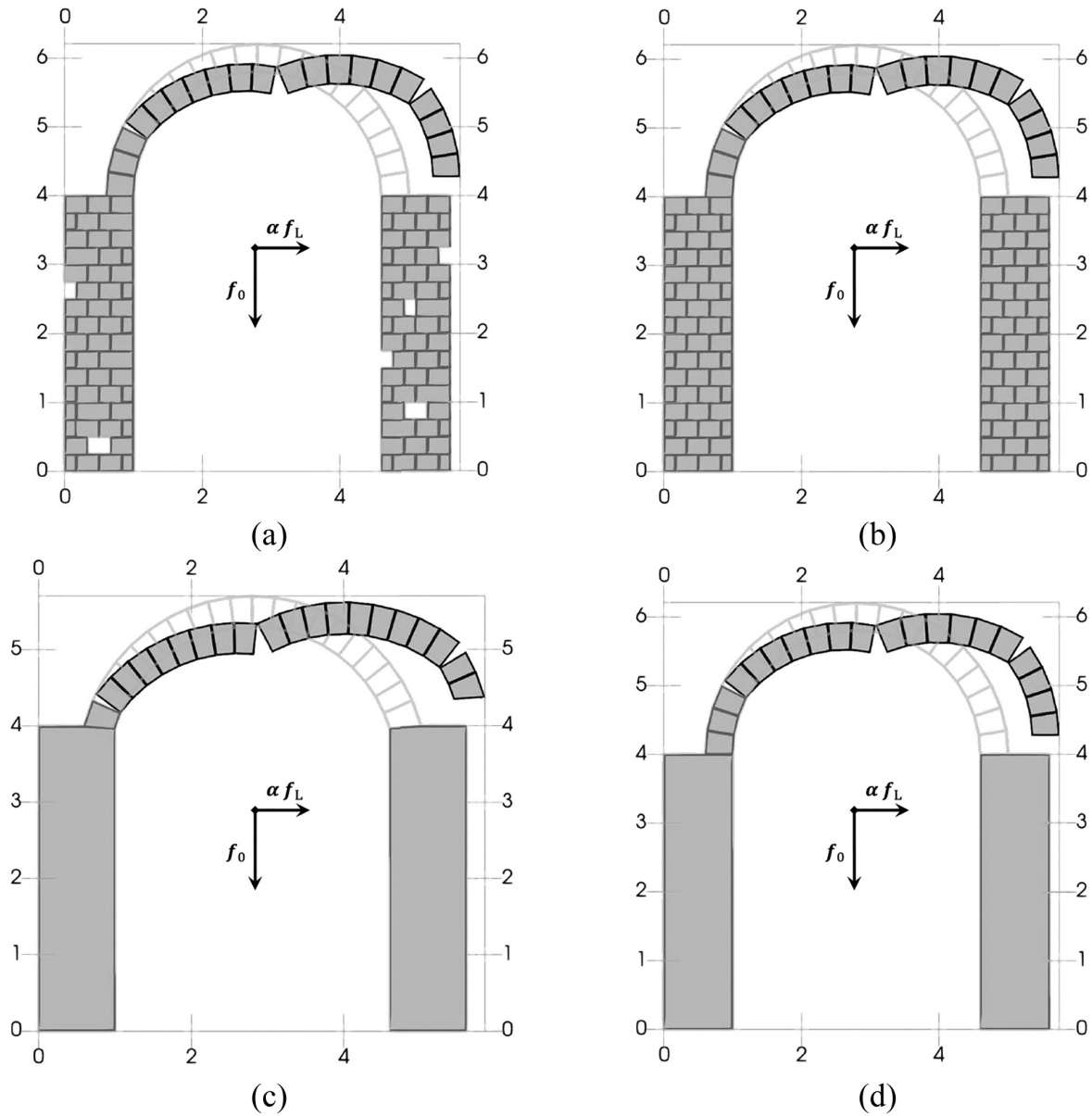


Figure 10. Combined collapse mechanisms involving hinging at the arch and sliding at the arch springs (grid in m): (a) IRR_500_20 and $\alpha = 0.0617$, (b) REG_500_20 and $\alpha = 0.0617$, (c) MON_375_20 and $\alpha = 0.0754$, and (d) MON_500_20 and $\alpha = 0.0617$.

previous case of shallow arches, the failure is localized at the spring, and due to the relatively smaller thrust (i.e. obtained from an increased arch rise), it slides only involving the springing block. While in the case of shallow arch, the monolithic texture of the pier alternates the previous behaviour as there is no discretization at its top. Low-friction values are also required for the appearance of such failure mode.

Another combined failure mode involving the sliding of masonry blocks is shown in Figure 11. This type of collapse mechanism involves both the arch and one pier. A rotation hinge opens at the intrados of the arch near one of its springs, then, there is sliding of the arch blocks near its key, and finally, the opposite side of the structure rotates about a second rotation hinge that appears at the base of the pier. This collapse mechanism is characteristic of highly pointed arches (arch shallowness of 0.866). As a different mass is mobilized when this failure mode occurs (notice that for the discretized piers, the lower left blocks of the right piers do not move), different values of collapse multipliers are computed for the various buttressed arches simulated. Once again it

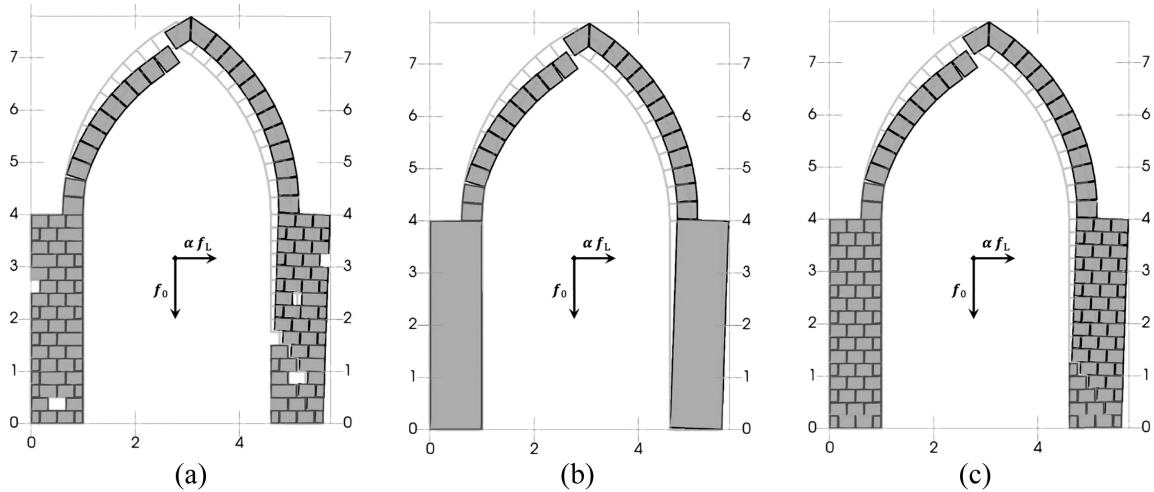


Figure 11. Combined collapse mechanisms involving hinging and sliding at both the arch and pier (grid in m): (a) IRR_866_20 and $\alpha = 0.1057$, (b) MON_866_20 and $\alpha = 0.1268$, and (c) REG_866_20 and $\alpha = 0.1122$.

is worth highlighting the fact that this mechanism is only found when low values of friction are assumed, which are necessary for the sliding of the masonry blocks near the arch key.

Last, a pure rotation collapse mechanism which involved both the arch and one pier was also detected. It is characterized by two rotation hinges at the arch intrados near its springs, one rotation hinge at the arch extrados near its key and a fourth rotation hinge located at the base of one pier. This failure mode is characteristic of the buttressed arches where a medium- to high-friction value was adopted. All buttressed arches with pier void texture presented a pure rotation collapse mechanism regardless of the values adopted for the rest of parameters for the horizontal live load case. The relatively high-friction value prevents sliding between blocks and forces the formation of a pure rotation mechanism through the opening of aforementioned hinges. This is the only failure mode that could be detected if Heyman's assumptions were to be strictly applied.

4.3. Collapse multipliers for the concentrated vertical live load applied at mid-span case

The box/swarm plots of the collapse multipliers obtained for the concentrated vertical live load applied at mid-span are shown in Figure 13. In accordance with what was observed for the previously discussed load case, a positive relation can be observed between arch shallowness and friction values with respect to collapse multiplier values. Higher collapse multipliers are generally obtained for pointed arches than for semi-circular or shallow arches. Especially, for this load scenario, the collapse multiplier values obtained for the semi-circular arches seem to be slightly inferior in comparison with those obtained from the shallow arches, which is counterintuitive. The trend observed for the different levels of the friction parameter is as expected, in other words, the higher the friction value, the higher the collapse multiplier. Also in terms of pier texture, the values obtained correspond to the hypothesis that piers following the "rule of art" (monolithic and regular texture) would result in stronger structures than those that do not follow those principles (irregular and voids textures).

Similar data spread is observed within the pier groups. Slightly higher variability can be seen for the low friction models in comparison with medium- and high-friction ones. Pointed arches with a shallowness value of 0.707 present a relatively smaller data spread in comparison with the rest of arch geometries. Table 2 presents the computed IQRs for the concentrated vertical live load applied at mid-span case.

In the case of the Pareto chart in Figure 13(b) with the threshold at 2.1, again it is observed that each single term of this chart has a significant importance with texture being the highest. Whereas regarding two-way interactions, the highest significance obtained is the one related to the combination texture-shallowness. Although, the combination shallowness-friction shows a similar significance but slightly lower.

For the concentrated live load applied at mid-span scenario, only one outlier was detected which was related to the pointed arches group, 0.707, corresponding to the voids pier texture in combination with low-friction value.

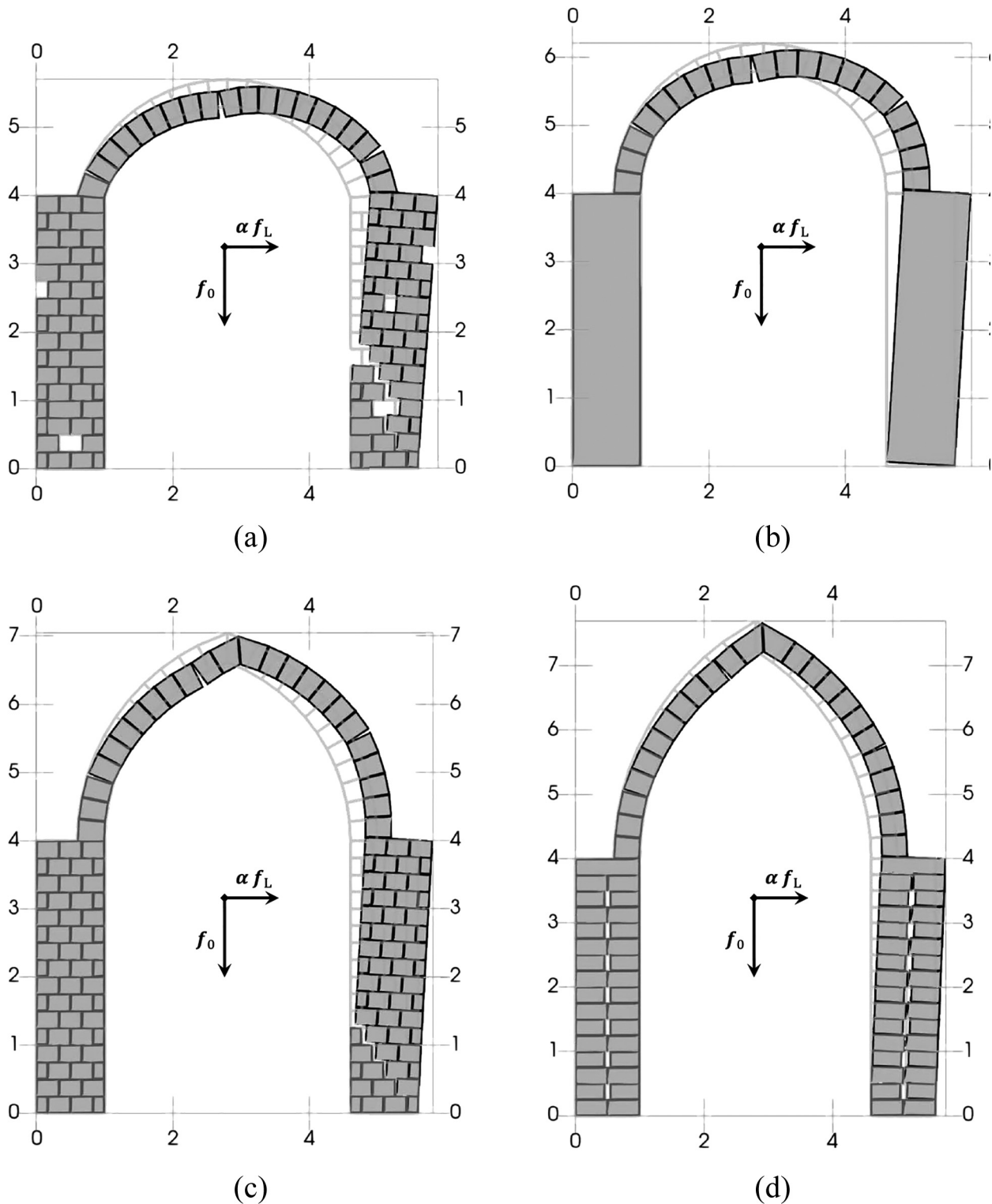


Figure 12. Pure rotation collapse mechanisms involving hinging at both the arch and the pier (grid in m): (a) IRR_375_30 and $\alpha = 0.0723$, (b) MON_500_40 and $\alpha = 0.1090$, (c) REG_707_30 and $\alpha = 0.1127$, and (d) VOD_866_40 and $\alpha = 0.0991$.

4.4. Collapse mechanisms for the concentrated vertical live load applied at mid-span case

In terms of failure modes, three different collapse mechanisms were observed for the concentrated vertical live load applied at mid-span case models:

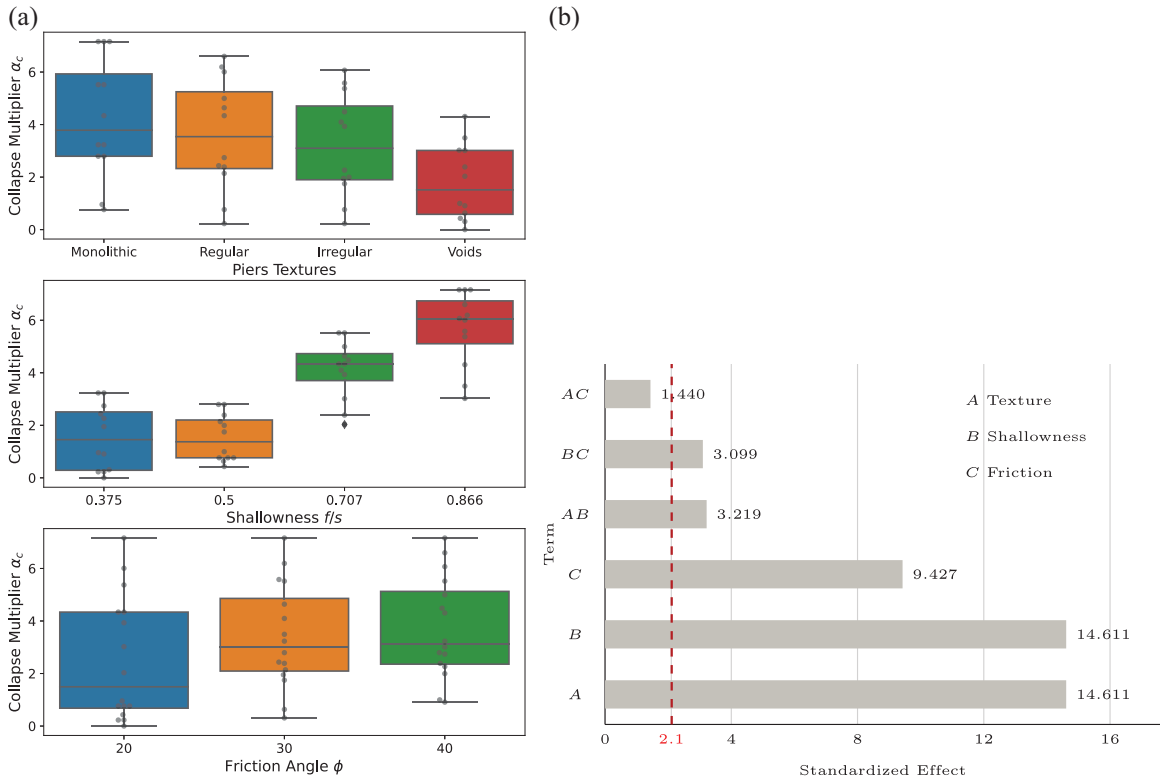


Figure 13. (a) Box plot and swarm plot of all collapse multipliers and (b) the Pareto chart of standardized effects for the concentrated vertical live load applied at mid-span case.

Table 2. Interquartile ranges (IQRs) for all parameter levels for the concentrated vertical live load applied at mid-span case.

Parameter	Level	IQR	Mean	Coef. var.	Min.	Max.
Piers textures	Monolithic	3.13442	4.21906	0.54385	0.76347	7.15929
	Regular	2.92367	3.62221	0.58960	0.22888	6.59726
	Irregular	2.80774	3.20732	0.61185	0.22888	6.06933
	Voids	2.43201	1.79462	0.79965	0.00029	4.30723
Shallowness f/s	0.866	1.63223	5.67646	0.24776	3.02301	7.15929
	0.707	1.02678	4.10822	0.27271	2.03132	5.51903
	0.500	1.43927	1.51787	0.58347	0.43035	2.79468
	0.375	2.22238	1.54066	0.80028	0.00029	3.23175
Friction angle ϕ	40	2.77096	3.71688	0.52055	0.90966	7.15929
	30	2.76598	3.39442	0.58513	0.30840	7.15929
	20	3.65854	2.52111	0.93765	0.00029	7.15929

1. Symmetrical combined hinging at the arch and sliding at the arch springs.
2. Symmetrical pure hinging at both arch and piers, also known as Mascheroni mechanism [58].
3. Pure hinging at both arch and pier.

The pure arch mechanism found for the concentrated live load applied at mid-span models is characterized by the opening of three hinges at the arch (two at their intrados near the arches' haunches and one at their extrados in their key) and sliding at both arch springs. This mechanism is symmetrical, and since the piers do not participate, it can appear on monolithic and regular texture piers, as well as in irregular texture piers as shown in Figure 14. A typical characteristic of this failure mode is the low values of friction that are necessary to allow sliding of the arch on top of the piers. Once again, as the piers are not involved in the failure mode, same collapse multiplier values are obtained for similar arch geometries ($\alpha_c = 0.7635$ for semi-circular arches, $\alpha_c = 0.9577$ for shallow arches, and $\alpha_c = 4.3387$ for pointed arches with a shallowness value of 0.707). It was

Table 3. Interquartile ranges (IQRs) for all parameter levels for the concentrated vertical live load applied at quarter-span case.

Parameter	Level	IQR	Mean	Coef. var.	Min.	Max.
Piers textures	Monolithic	1.25351	2.21709	0.41253	0.71662	3.78630
	Regular	0.98695	2.02501	0.38971	0.71662	3.46972
	Voids	1.28385	1.22262	0.64046	0.00039	2.51576
	Irregular	0.75026	1.86855	0.37503	0.71662	3.13270
Shallowness f/s	0.375	1.48153	1.63901	0.62841	0.00039	3.03515
	0.500	1.26665	1.38185	0.54983	0.45353	2.45827
	0.707	1.03101	2.34715	0.33515	1.33661	3.78630
	0.866	1.25726	1.96527	0.29889	1.29781	2.72308
Friction angle ϕ	40	0.60096	2.47495	0.30717	0.94880	3.78630
	20	0.60341	1.06109	0.43225	0.00039	1.63085
	30	0.56162	1.96391	0.33958	0.41923	3.03515

possible to capture this failure mode owing to the capabilities of the implemented upper-bound limit analysis approach.

Medium- or high-friction values though led to the appearance of a different symmetric failure mode, which is presented in Figure 15. This collapse mechanism involves both piers and the arch. It is characterized by the opening of five rotation hinges: one at the arch extrados key, two at the arch intrados haunches, and two more at each pier base. All buttressed arches with pier void texture presented a Mascheroni collapse mechanism regardless of the values adopted for the rest of parameters for the vertical live load applied at mid-span case. This mechanism can only appear on the models where symmetric loading conditions and symmetric geometrical conditions are preserved, namely, monolithic, regular, and voids texture pier buttressed arches.

Last, those failure modes involving pure rotation hinges at both the arch and the piers that do not satisfy the symmetric geometrical conditions (irregular texture piers) developed an asymmetrical four hinges collapse mechanism as presented in Figure 16. In this collapse mechanism, a rotation hinge appears at the intrados near both of the arch springs, a third hinge develops at the arch extrados key and a final hinge is created at the opposite pier base.

4.5. Collapse multipliers for the concentrated vertical live load applied at quarter-span case

The box/swarm plots of the collapse multipliers obtained for the concentrated vertical live load applied at mid-span are shown in Figure 17. The trend of collapse multiplier values for the pier texture and friction value is similar as those found in previously discussed load case scenarios. On the other hand, although pointed arches present higher α_c values than shallow and semi-circular ones, it can be observed for this load case that shallow arches and pointed (0.707) arches generally result in higher collapse multipliers than semi-circular and pointed (0.866) arches, respectively. This may be explained based on the different failure modes encountered and discussed in the following section.

Under the concentrated vertical live load applied at quarter-span scenario, the data spread of the monolithic pier models turned out to be slightly larger than for the rest of pier textures analyzed. Similarly, shallow arches showed a higher variability for the collapse multiplier values obtained with respect to the rest of arch geometries. All levels of friction value resulted in similar data spread. Table 3 presents the computed IQRs for the concentrated vertical live load applied at quarter-span case.

The outliers observed for this last load case scenario corresponded only to the friction parameter. Two outliers resulted from the middle-friction value group, namely, models with voids pier texture and shallow or semi-circular arches. Similarly, for the high-friction value group, the models with voids pier texture and shallow or semi-circular arches turned out to be outliers. All these four outliers were found below their corresponding group lower fences. On the other hand, one last outlier (related to the high-friction group and corresponding to the monolithic pier and pointed arch 0.707) was found above its upper fence.

For this scenario assessing the Pareto chart in Figure 17(b) with the threshold at 2.1, again it is observed that each single term of this chart has a significant importance but contrary to the others friction being the highest. Furthermore, in contrast to the other scenarios, all the single and two-way interaction terms show significance of the response. The highest among the two term interactions is achieved for the one between texture and shallowness followed by texture-friction and last the one between shallowness and friction.

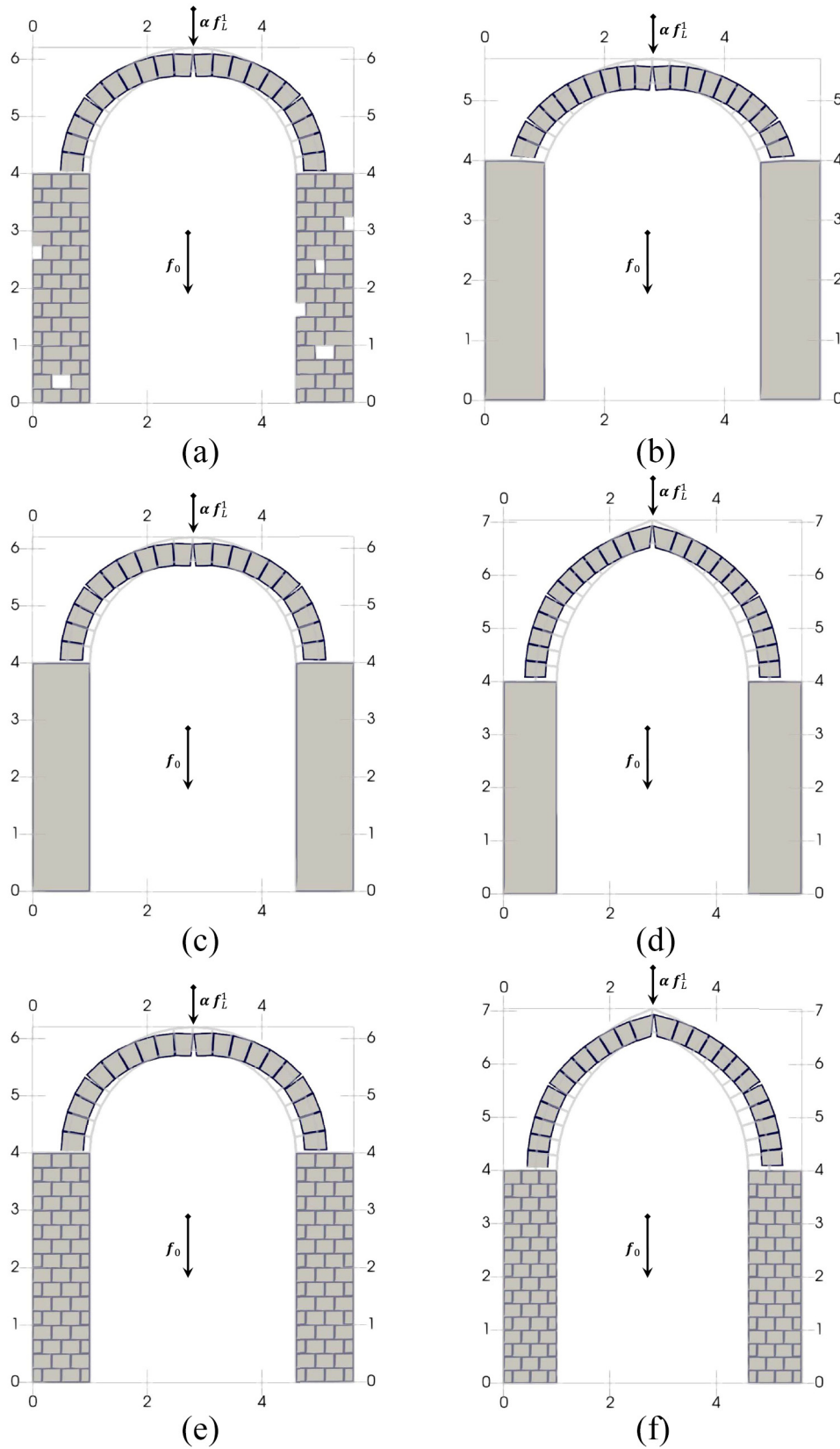


Figure 14. Pure arch mechanisms, sliding at springs and three hinge openings (grid in m): (a) IRR_500_20 and $\alpha_c = 0.7635$, (b) MON_375_20 and $\alpha_c = 0.9577$, (c) MON_500_20 and $\alpha_c = 0.7635$, (d) MON_707_20 and $\alpha_c = 4.3387$, (e) REG_500_20 and $\alpha_c = 0.7635$, and (f) REG_707_20 and $\alpha_c = 4.3387$.

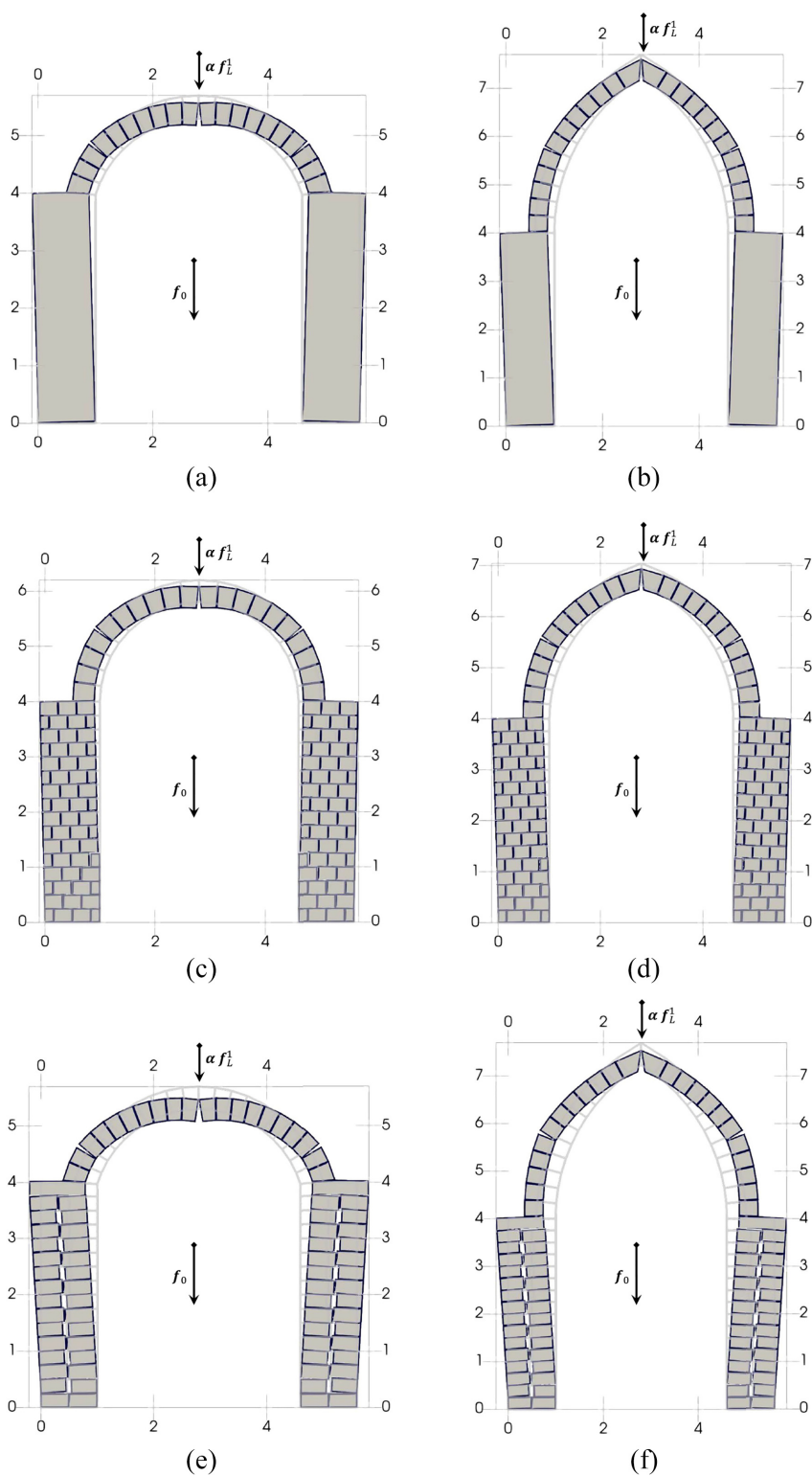


Figure 15. Symmetric pure hinging (Mascheroni) mechanisms involving both piers (grid in m): (a) MON_375_30 and $\alpha_c = 3.2317$, (b) MON_866_40 and $\alpha_c = 7.1593$, (c) REG_500_30 and $\alpha_c = 2.1414$, (d) REG_707_40 and $\alpha_c = 4.9966$, (e) VOD_375_20 and $\alpha_c = 0.00029$, and (f) VOD_866_40 and $\alpha_c = 4.3072$.

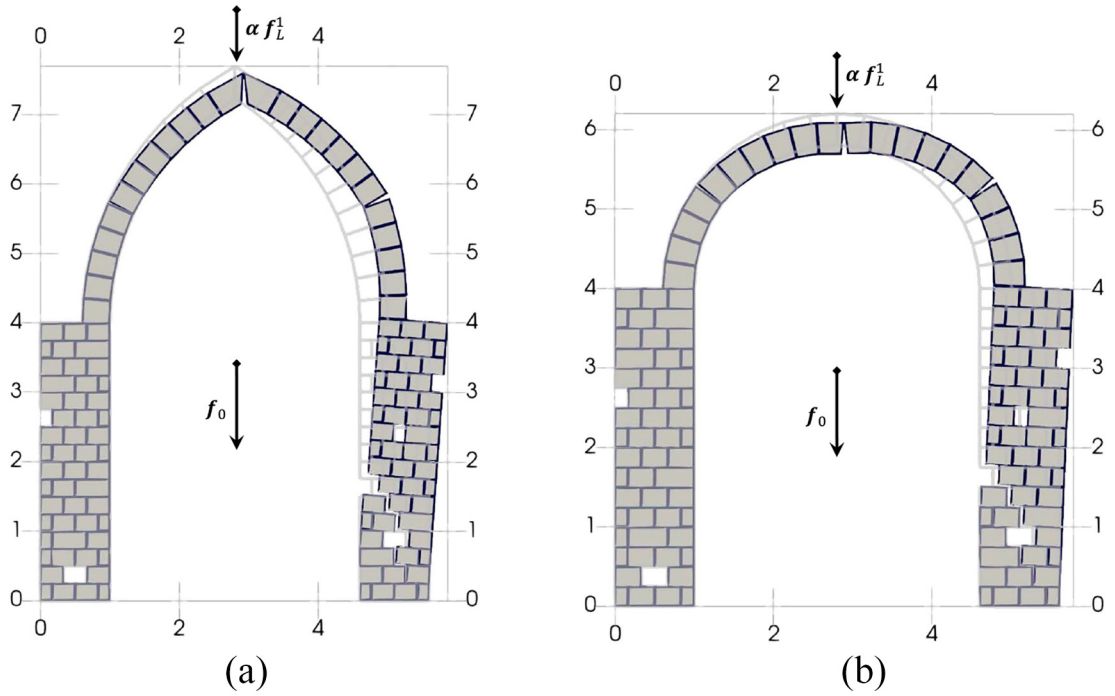


Figure 16. Pure rotation collapse mechanisms involving hinging at both the arch and pier (grid in m): (a) IRR_866_40 and $\alpha_c = 6.0693$ and (b) IRR_500_30 and $\alpha_c = 1.7484$.

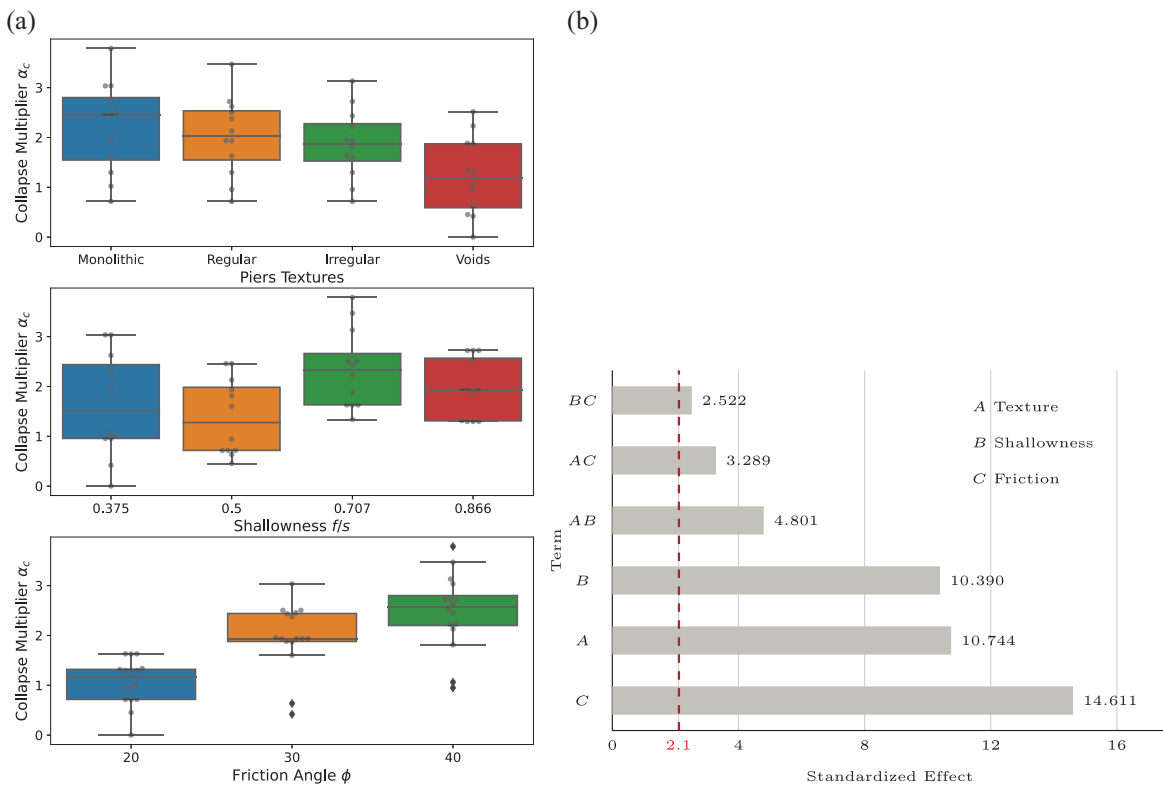


Figure 17. (a) Box plot and swarm plot of all collapse multipliers and (b) the Pareto chart of standardized effects for the concentrated vertical live load applied at quarter-span case.

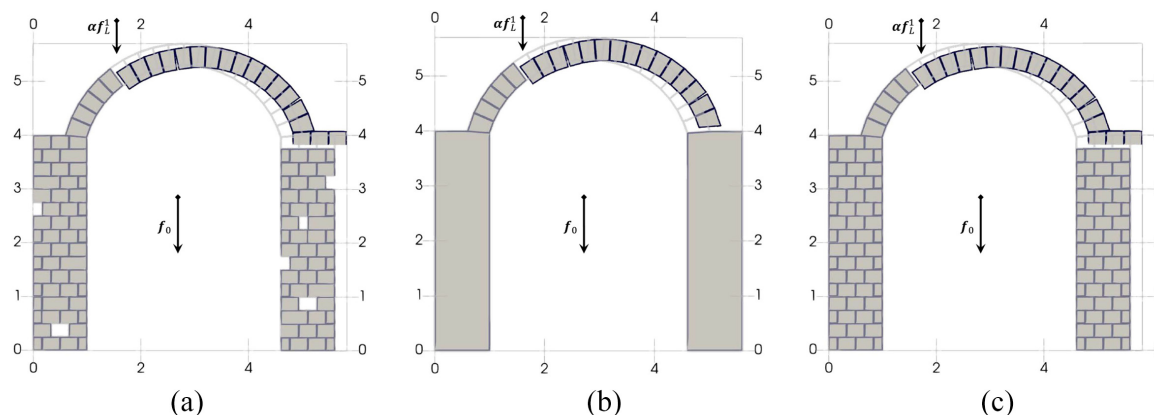


Figure 18. Pure sliding collapse mechanism involving the blocks under the applied concentrated live load and the first row of pier blocks (grid in m): (a) IRR_375_20 and $\alpha_c = 0.9570$, (b) MON_375_20 and $\alpha_c = 1.0227$, and (c) REG_375_20 and $\alpha_c = 0.9570$.

4.6. Collapse mechanisms for the concentrated vertical live load applied at quarter-span case

In terms of failure modes, four different collapse mechanisms were observed also for the concentrated vertical live load applied at quarter-span case models:

1. Pure sliding.
2. Combined hinging and sliding at the arch spring.
3. Combined hinging and sliding near the arch key.
4. Pure hinging at both arch and pier.

The pure sliding mechanism is perhaps the most interesting failure mode capture with the implemented upper-bound limit approach of this paper. It occurs only within the arch (for the monolithic pier case) or within the arch and upper block course of one pier (for the regular and irregular pier textures). The first sliding between blocks appears at quarter-span, location where the concentrated vertical load is applied, whereas that a second sliding happens at the arch spring (for the monolithic case) or at the first masonry course of the opposite pier as shown in Figure 18. As only the arch and upper course of one pier are involved within this failure mode, the collapse multiplier computed is the same regardless of the pier discretization ($\alpha_c = 0.9570$). A necessary condition for this failure mode to arise is having a low-friction value which does not prevent the sliding between blocks, in combination with a shallow arch that exerts enough horizontal thrust at its spring.

The other three mechanisms found for the concentrated vertical load applied at quarter-span are similar to those described in the previous sections. See Figures 19–21 in comparison with Figures 10–12 or 16, respectively.

4.7. Computational efficiency

Last, in this section, the computational burden and the efficiency of this study utilizing the in-house ALMA code is summarized. All the analyses have been run within the same personal computer machine with the following characteristics: Intel® Core™ i7-10750H CPU 2.60 GHz and 32 GB or RAM. The summary of runtime is given in Table 4, where the time (in seconds) is averaged for every three levels of friction and the results consist the runtime for all the live load scenarios. The number of blocks varies from 22 to 136, while the time taken per analysis varies between 0.57 and 43.8 s.

5. Conclusion

In this paper, a parametric analysis based on the implementation of an upper-bound limit analysis has been performed to study the structural response and failure modes of masonry arches over piers. The parameters taken into account were the pier texture (monolithic, regular, irregular, and voids), arch shallowness (0.375, 0.500, 0.707, and 0.866), and friction angle values (20° , 30° , and 40°). Furthermore, the buttressed arches were

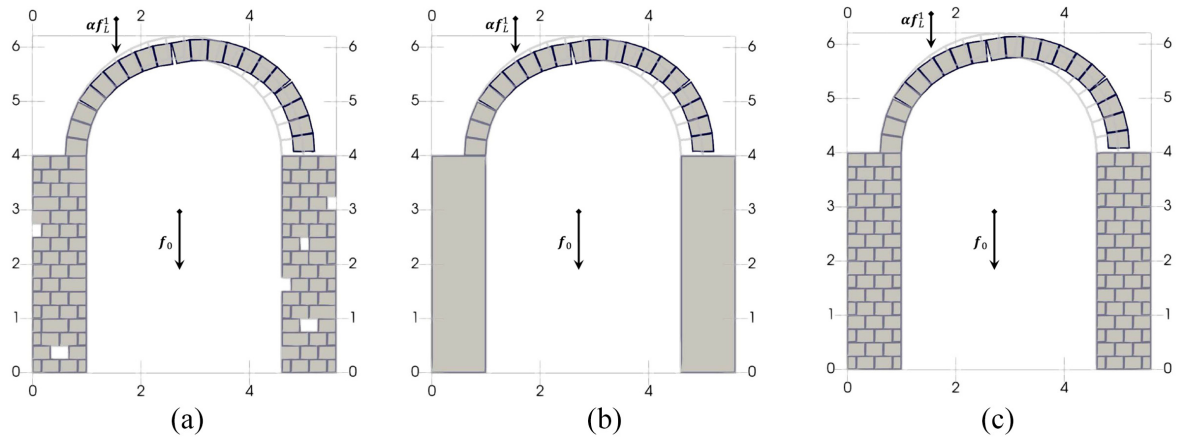


Figure 19. Combined hinging and sliding at arch spring collapse mechanism (grid in m): (a) IRR_500_20 and $\alpha_c = 0.7166$, (b) MON_500_20 and $\alpha_c = 0.7166$, and (c) REG_500_20 and $\alpha_c = 0.7166$.

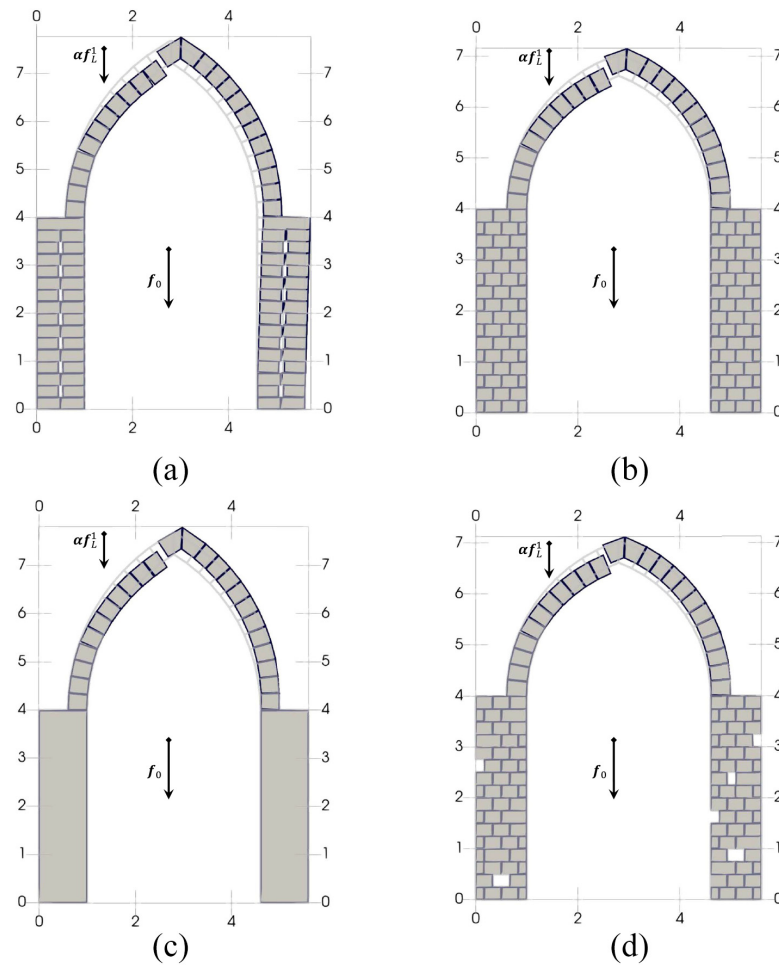


Figure 20. Combined hinging and sliding near the arch key collapse mechanism (grid in m): (a) VOD_866_40 and $\alpha_c = 2.5158$, (b) REG_707_30 and $\alpha_c = 2.5049$, and (c) MON_866_40 and $\alpha_c = 2.7231$. (d) REG_707_20 and $\alpha_c = 1.6308$.

analyzed under three different load case scenarios, namely, horizontal live load, vertical live load applied at mid-span, and vertical live load applied at quarter-span. All load scenarios considered the self-weight of the

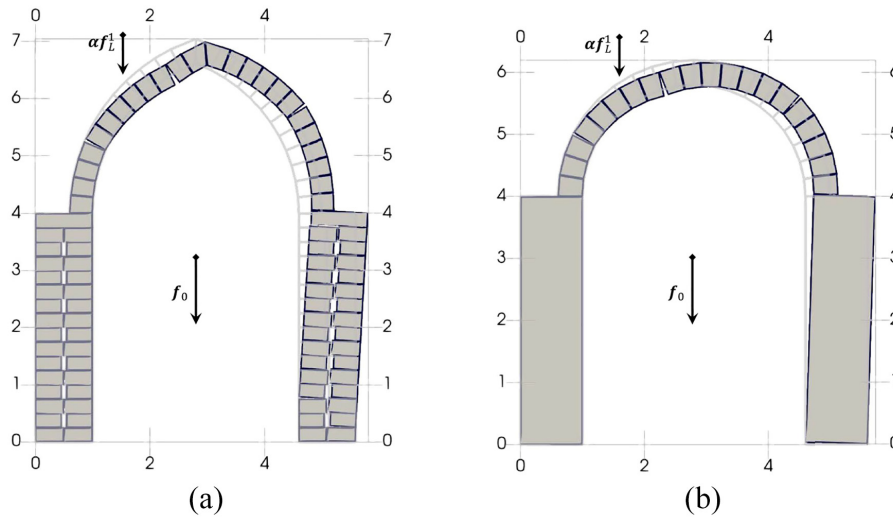


Figure 21. Pure rotation collapse mechanisms involving hinging at both the arch and the pier (grid in m): (a) VOD_707_40 and $\alpha_c = 2.2322$ and (b) MON_500_30 and $\alpha_c = 2.4583$.

Table 4. Computational time taken for the analysis.

Texture	Shallowness	No. blocks	Hor	Average time (s) for:	
				VerMid	VerQua
MON	0.375	22	0.60	0.60	0.59
	0.500	22	0.58	0.57	0.57
	0.707	26	0.81	0.87	0.81
	0.866	26	0.80	0.84	0.79
REG	0.375	121	32.40	32.63	31.93
	0.500	121	30.63	31.63	31.47
	0.707	125	34.37	35.90	34.30
	0.866	125	34.17	35.47	34.17
IRR	0.375	132	39.37	39.33	39.93
	0.500	132	40.07	40.33	38.90
	0.707	136	43.80	43.10	42.40
	0.866	136	41.93	43.03	41.17
VOD	0.375	82	9.61	9.39	9.54
	0.500	82	9.68	9.73	9.19
	0.707	86	11.03	11.10	10.53
	0.866	86	11.10	11.03	10.50

Hor: horizontal live load; VerMid: vertical live load at mid-span; VerQua: vertical live load at quarter-span.

structure as well. A full composite design was used to combine the different levels of each parameter for every load scenario, thus obtaining a total of 144 different models.

The main conclusions drawn from the results obtained are:

- All parameters studied (pier texture, arch shallowness, and friction values) showed a significant effect on the structural response of buttressed arches regardless of the load scenario. The structural integrity and the soundness of piers as a result of the “rule of art” provide a crucial aspect in the overall behavior and they are key aspects to be considered during inspection and assessment of such structures. Furthermore, the disposition of such blocks in the formation of different masonry arrangements (texture) plays an important role on the outcome that is not taken into account with approaches that consider masonry material as a homogeneous media.
- Different load scenarios account for unique collapse mechanisms, i.e. only-arch mechanism for the vertical live load applied at mid-span and pure sliding mechanism for the vertical live load applied at quarter-span.

- Some mechanisms, namely, pure rotation and combined hinging-sliding, are common to all three different load scenarios analyzed. In such cases, it can be stated that accurate and proper tools of assessment are necessary while studying and analyzing the behavior of such complex and intricate structures.






Funding

The author(s) disclosed receipt of the following financial support for the research, authorship, and/or publication of this article: This work is supported by Italian Ministry of University and Research PRIN 2017, project no. 2017HFPKZY (B88D19001130001); Sapienza Research Grant “Progetti Grandi” 2021 (B85F21008380001); Sapienza Research Grant “Progetti Medi” 2022. The financial support of Fondazione di Sardegna, Italy through grant Surveying, modeling, monitoring and rehabilitation of masonry vaults and domes, that is, Rilievo, modellazione, monitoraggio e risanamento di volte e cupole in muratura (RMMR) (CUP code: F72F20000320007).

Data availability statement

Some or all data, models, or code generated or used during the study are available in a repository or online in accordance with funder data retention policies.

ORCID iDs

Alejandro Jimenez Rios  <https://orcid.org/0000-0003-4470-255X>
 Bledian Nela  <https://orcid.org/0000-0002-7861-2029>
 Marco Pingaro  <https://orcid.org/0000-0002-7037-8661>
 Emanuele Reccia  <https://orcid.org/0000-0003-0499-4295>
 Patrizia Trovalusci  <https://orcid.org/0000-0001-7946-3590>

References

- [1] Milani, G, and Valente, M. Failure analysis of seven masonry churches severely damaged during the 2012 Emilia-Romagna (Italy) earthquake: non-linear dynamic analyses vs conventional static approaches. *Eng Fail Anal* 2015; 54: 13–56, <https://www.sciencedirect.com/science/article/pii/S1350630715001041>
- [2] Foraboschi, P. Church of San Giuliano di Puglia: seismic repair and upgrading. *Eng Fail Anal* 2013; 33: 281–314, <https://www.sciencedirect.com/science/article/pii/S1350630713001994>
- [3] Elyamani, A, Roca, P, Caselles, O, et al. Seismic safety assessment of historical structures using updated numerical models: the case of Mallorca cathedral in pain. *Eng Fail Anal* 2017; 74: 54–79, <https://www.sciencedirect.com/science/article/pii/S1350630716307567>
- [4] Bruggi, M, Lógó, B, and Deák, Z. Funicular analysis of ribbed masonry vaults: a case study. *Int J Archit Herit* 2021; 16: 1809–1823, <https://www.tandfonline.com/doi/abs/10.1080/15583058.2021.1910879?journalCode=uarc20>
- [5] Saloustros, S, Pelá, L, Roca, P, et al. Numerical analysis of structural damage in the church of the Poblet Monastery. *Eng Fail Anal* 2015; 48: 41–61, <https://www.sciencedirect.com/science/article/pii/S135063071400315X>
- [6] Saydan, M, Unal, A, Keskin, US, et al. An investigation of the current situation of the Mısırlıoğlu bridge and possible damages after freeze-thaw by using finite elements analysis, Sille – Konya (Central Anatolia, Turkey). *Eng Fail Anal* 2020; 117: 104788, <https://www.sciencedirect.com/science/article/pii/S1350630719319314>
- [7] Valente, M, and Milani, G. Earthquake-induced damage assessment and partial failure mechanisms of an Italian medieval castle. *Eng Fail Anal* 2019; 99: 292–309, <https://www.sciencedirect.com/science/article/pii/S1350630718313207>
- [8] Peña, F, and García, N. Numerical evaluation of the seismic behavior of façades of Mexican colonial churches. *Eng Fail Anal* 2016; 62: 164–177, <https://www.sciencedirect.com/science/article/pii/S1350630716300115>
- [9] Preciado, A, Santos, JC, Silva, C, et al. Seismic damage and retrofitting identification in unreinforced masonry churches and bell towers by the September 19, 2017 (mw = 7.1) Puebla-Morelos earthquake. *Eng Fail Anal* 2020; 118: 104924, <https://www.sciencedirect.com/science/article/pii/S1350630720314485>
- [10] Valente, M, Barbieri, G, and Biolzi, L. Seismic assessment of two masonry Baroque churches damaged by the 2012 Emilia earthquake. *Eng Fail Anal* 2017; 79: 773–802, <https://www.sciencedirect.com/science/article/pii/S1350630716307609>
- [11] Valente, M, and Milani, G. Damage assessment and partial failure mechanisms activation of historical masonry churches under seismic actions: Three case studies in Mantua. *Eng Fail Anal* 2018; 92: 495–519, <https://www.sciencedirect.com/science/article/pii/S1350630718304126>
- [12] Alexakis, H, and Makris, N. Hinging mechanisms of masonry single-nave barrel vaults subjected to lateral and gravity loads. *J Struct Eng* 2017; 143(6): 04017026, <https://ascelibrary.org/doi/abs/10.1061/%28ASCE%29ST.1943-541X.0001762>

- [13] Gizzi, FT, Sileo, M, Biscione, M, et al. The conservation state of the Sassi of Matera site (Southern Italy) and its correlation with the environmental conditions analysed through spatial analysis techniques. *J Cult Herit* 2016; 17: 61–74, <https://www.sciencedirect.com/science/article/pii/S1296207415000928>
- [14] Gallipoli, M, and Lupo, M. *Caratterizzazione dei terreni e risposta sismica locale dell'area urbana di Matera (Tecniche speditive per la stima dell'amplificazione sismica e della dinamica degli edifici Studi teorici ed applicazioni professionali a cura di Marco Mucciarelli)*. Rome: ARACNE Editrice, 2012, pp. 323–342.
- [15] Baggio, C, and Trovalusci, P. Stone assemblies under in-plane actions. Comparison between nonlinear discrete approaches. *Comput Methods Struct Mason* 1995; 3: 184–193.
- [16] Efesiou, I. Constructional analysis of the local structural system of the historic settlement of Anavatos in Chios island. In: *International seminar of restoration of historic buildings in seismic areas: the case of settlements in the Aegean*, Lesvos Island, 24–26 May 2001, pp. 149–154. Athens: European Centre on Prevention and Forecasting for Earthquakes.
- [17] UNESCO World Heritage Centre. The Sassi and the Park of the Rupestrine churches of Matera, 2022, <https://whc.unesco.org/en/list/670/>
- [18] Giuffrè, A, and Carocci, C. *Codice di pratica per la sicurezza e la conservazione dei sassi di matera*. Venice: La Baitta, 1997.
- [19] Carocci, CF. *Guidelines for the safety and preservation of historical centres in seismic areas (Historical constructions)*. Guimarães: University of Minhi, 2001.
- [20] De Luca, A, Giordano, A, and Mele, E. A simplified procedure for assessing the seismic capacity of masonry arches. *Eng Struct* 2004; 26(13): 1915–1929, <https://www.sciencedirect.com/science/article/pii/S0141029604002263>
- [21] Rios, AJ, Pingaro, M, Reccia, E, et al. Statistical assessment of in-plane masonry panels using limit analysis with sliding mechanism. *J Eng Mech* 2022; 148(2): 04021158, <https://ascelibrary.org/doi/abs/10.1061/%28ASCE%29EM.1943-7889.0002061>
- [22] Pulatsu, B, Erdogmus, E, Bretas, EM, et al. In-plane static response of dry-joint masonry arch-pier structures. In: *Proceedings of the Architectural Engineering Conference 2019*, Tysons, VA, 3–6 April 2019, pp. 240–248. Reston, VA: American Society of Civil Engineers, <https://ascelibrary.org/doi/abs/10.1061/9780784482261.028>
- [23] Dimitri, R, De Lorenzis, L, and Zavarise, G. Numerical study on the dynamic behavior of masonry columns and arches on buttresses with the discrete element method. *Eng Struct* 2011; 33(12): 3172–3188, <https://www.sciencedirect.com/science/article/pii/S0141029611003336>
- [24] Bagi, K. When Heyman's safe theorem of rigid block systems fails: non-Heymanian collapse modes of masonry structures. *Int J Solids Struct* 2014; 51(14): 2696–2705, <https://www.sciencedirect.com/science/article/pii/S0020768314001474>
- [25] Hua, Y, and Milani, G. Rigid block limit analysis of masonry arches with associated and non-associated slides. In: Milani, G, and Sarhosis, V (eds) *From corbel arches to double curvature vaults: analysis, conservation and restoration of architectural heritage masonry structures*. Cham: Springer, 2022, pp. 169–203.
- [26] Hua, Y, and Milani, G. Simple modeling of reinforced masonry arches for associated and non-associated heterogeneous limit analysis. *Comput Struct* 2023; 280: 106987, <https://www.sciencedirect.com/science/article/pii/S0045794923000172>
- [27] Gilbert, M, Casapulla, C, and Ahmed, H. Limit analysis of masonry block structures with non-associative frictional joints using linear programming. *Comput Struct* 2006; 84(13): 873–887, <https://www.sciencedirect.com/science/article/pii/S0045794906000356>
- [28] Zampieri, P, Amoroso, M, and Pellegrino, C. The masonry buttressed arch on spreading support. *Structures* 2019; 20: 226–236, <https://www.sciencedirect.com/science/article/pii/S2352012419300517>
- [29] Nela, B, Rios, AJ, Pingaro, M, et al. Limit analysis of locally reinforced masonry arches. *Eng Struct* 2022; 271: 114921.
- [30] Nela, B, Rios, AJ, Pingaro, M, et al. Masonry arches simulations using cohesion parameter as code enrichment for limit analysis approach. *Int J Mason Res Innov*. Epub ahead of print 5 May 2023. DOI: 10.1504/ijmri.2023.10053576.
- [31] Dimitri, R, and Tornabene, F. A parametric investigation of the seismic capacity for masonry arches and portals of different shapes. *Eng Fail Anal* 2015; 52: 1–34, <https://www.sciencedirect.com/science/article/pii/S1350630715000783>
- [32] Milani, G. Simple lower bound limit analysis model for masonry double curvature structures. *Comput Struct* 2022; 269: 106831, <https://www.sciencedirect.com/science/article/pii/S0045794922000918>
- [33] Heyman, J. The stone skeleton. *Int J Solids Struct* 1966; 2(2): 249–256, IN1–IN4, 257–264, IN5–IN12, 265–279, <https://www.scopus.com/inward/record.uri?eid=2-s2.0-0004942133&partnerID=40&md5=038571f2507293cb3e3733e941ba1f47>
- [34] Heyman, J. The safety of masonry arches. *Int J Mech Sci* 1969; 11(4): 363–382, IN3–IN4, 383–385
- [35] Heyman, J. *The masonry arch*. Hoboken, NJ: John Wiley and Sons, 1982.
- [36] DeJong, MJ, and Ochsendorf, J. Analysis of vaulted masonry structures subjected to horizontal ground motion. In: Aguilar, R, Torrealva, D, Moreira, S, et al. (eds) *Structural analysis of historical constructions*. Berlin: Springer, 2006, pp. 973–980.
- [37] Brandonisio, G, Angelillo, M, and De Luca, A. Seismic capacity of buttressed masonry arches. *Eng Struct* 2020; 215: 110661, <https://www.sciencedirect.com/science/article/pii/S0141029619353015>
- [38] Brandonisio, G, and De Luca, A. Analytical modelling for the seismic assessment of pointed arches supported by buttresses. *Int J Mason Res Innov* 2021; 6(4): 384–404, <https://www.inderscienceonline.com/doi/abs/10.1504/IJMRI.2021.118821>
- [39] Tiberti, S, Grillanda, N, Mallardo, V, et al. A genetic algorithm adaptive homogeneous approach for evaluating settlement-induced cracks in masonry walls. *Eng Struct* 2020; 221: 111073, <https://www.sciencedirect.com/science/article/pii/S0141029620321040>
- [40] Coccia, S, Di Carlo, F, and Rinaldi, Z. Collapse displacements for a mechanism of spreading-induced supports in a masonry arch. *Int J Adv Struct Eng* 2015; 7(3): 307–320, <https://doi.org/10.1007/s40091-015-0101-x>

- [41] Baggio, C, and Trovalusci, P. Limit analysis for no-tension and frictional three-dimensional discrete systems. *Mech Structures Mach* 1998; 26(3): 287–304.
- [42] Baggio, C, and Trovalusci, P. Collapse behaviour of three-dimensional brick-block systems using non-linear programming. *Struct Eng Mech* 2000; 10(2): 181–195.
- [43] Maier, G, and Nappi, A. A theory of no-tension discretized structural systems. *Eng Struct* 1990; 12(4): 227–234, <https://www.sciencedirect.com/science/article/pii/014102969090021J>
- [44] Drucker, DC. A more fundamental approach to plastic stress-strain relations. In: *Proceedings of the first US National Congress on Applied Mechanics*, Chicago, IL, 11–16 June 1951, pp. 487–491. New York: American Society of Mechanical Engineers.
- [45] Coulomb, CA. *Essai sur une application des règles de maximis & minimis à quelques problèmes de Statique, relatifs à l'architecture*. Paris: De l'Imprimerie Royale, 1773.
- [46] Drucker, DC. Coulomb friction, plasticity, and limit loads. *J Appl Mech Trans ASME* 1954; 21: 71–74.
- [47] Radenkovic, D. Théorèmes limites pour un matériau de Coulomb à dilation non standardisée. *C R Hebd Séances Acad Sci* 1961; 252(26): 4103.
- [48] Pepe, M, Sangirardi, M, Reccia, E, et al. Discrete and continuous approaches for the failure analysis of masonry structures subjected to settlements. *Front Built Environ* 2020; 6: 43.
- [49] Pepe, M. *Numerical modeling for masonry: ALMA 2.0, a computational code for the limit analysis of historical masonry structures*. PhD Thesis, Sapienza University of Rome, Rome, 2020.
- [50] MOSEK ApS. Mosek optimizer API for Python 9.3.18, 2022, <https://docs.mosek.com/latest/pythonapi/index.html>
- [51] Ahrens, J, Geveci, B, and Law, C. 36 - Paraview: an end-user tool for large-data visualization. In: Hansen, CD, and Johnson, CR (eds) *Visualization handbook*. Burlington, MA: Butterworth-Heinemann, 2005, pp. 717–731.
- [52] Romano, A. *Modelling, analysis and testing of masonry structures*. PhD Thesis, Università degli Studi di Napoli Federico II, Naples, 2006, <http://www.fedoa.unina.it/id/eprint/675>
- [53] Aita, D, Barsotti, R, and Bennati, S. Equilibrium of pointed, circular, and elliptical masonry arches bearing vertical walls. *J Struct Eng* 2012; 138(7): 880–888.
- [54] Lengyel, G, and Bagi, K. Horizontal reaction components of pointed vaults. *Int J Mason Res Innov* 2016; 1(4): 398–420.
- [55] Rios, AJ, Nela, B, Pingaro, M, et al. Rotation and sliding collapse mechanisms for in plane masonry pointed arches: statistical parametric assessment. *Eng Struct* 2022; 262: 114338, <https://www.sciencedirect.com/science/article/pii/S0141029622004540>
- [56] Rahman, A, and Ueda, T. Experimental investigation and numerical modeling of peak shear stress of brick masonry mortar joint under compression. *J Mater Civ Eng* 2014; 26(9): 04014061.
- [57] Shipeng, C, and Katalin, B. Crosswise tensile resistance of masonry patterns due to contact friction. *Proc R Soc A* 2020; 476: 20200439, <https://royalsocietypublishing.org/doi/10.1098/rspa.2020.0439>
- [58] Sinopoli, A. The role of geometry in the theories on vaulted structures by Lorenzo Mascheroni (1785). In: *Proceedings of the first international congress on construction history*, vol. 3, Madrid, 20–24 January 2003, pp. 1865–1873. Madrid: Instituto Juan de Herrera, Escuela Técnica Superior de Arquitectura.